# 3D BIOPRINTING OF OSTEOCHONDRIAL INTERFACE TISSUE

by

EFSUN ŞENTÜRK

Submitted to the Graduate School of Engineering and Natural Sciences

in partial fulfillment of the requirements for the degree of Master of Science.

Sabanci University

August 2022

# ABSTRACT


3D BIOPRINTING OF OSTEOCHONDRIAL INTERFACE TISSUE

EFSUN ŞENTÜRK

MATERIALS SCIENCE AND NANO ENGINEERING MSc. THESIS,
JULY 2022

Thesis Supervisor: Prof. Dr. Bahattin Koç

Keywords: Hybrid 3D Bioprinting, In-Situ Crosslink, Osteochondral Interface, Tyramine-Conjugated, Alginate, Carboxymethylcellulose

Recent advancements in tissue engineering have demonstrated the great potential for fabrication of three-dimensional synthetic tissue structures such as cartilage and bone. However, the achievement of structural integrity between different tissues and fabrication of tissue interfaces are still great challenges. In this thesis, *in situ* crosslinked hybrid multi-material 3D bioprinting approach was used for the fabrication of hydrogel structures based on an aspiration-on-demand capillary method. Different cell-laden hydrogels were extruded in the same microcapillary glass and deposited in the desired geometrical arrangement. Alginate and carboxymethyl cellulose were modified with tyramine to enhance cell bioactivity and mechanical properties of Mesenchymal Stem Cells (MSC)-laden bioinks. Hydrogels were prepared for extrusion by gelling in microcapillary glass utilizing an in-situ crosslink approach using ruthenium (Ru) and sodium persulfate (SPS) photo-initiating mechanisms under visible light. The developed bioinks are then bioprinted in precise gradient composition for cartilage-bone tissue interface using aspiration-extrusion microcapillary bioprinting technique. The biofabricated constructs were co-cultured in chondrogenic/osteogenic culture media for

three weeks. After differentiation of MSC cells in 21-day incubation, histology, immunohistochemistry, and a live/dead test for the bioprinted structure were carried out. The results of cartilage and bone formation analysis based on cell alignment and histological evaluation successfully revealed that mechanical cues, in conjunction with chemical cues, showed MSC to differentiate into chondrogenic and osteogenic tissues.

# ÖZET


3B BİYOBASIM İLE OSTEOKONDRAL ARAYÜZ DOKUSU

EFSUN ŞENTÜRK

MALZEME BİLİMİ VE NANO MÜHENDİSLİK YÜKSEK LİSANS TEZİ,
TEMMUZ 2022

Tez Danışmanı: Prof. Dr. Bahattin Koç

Anahtar Kelimeler: Hibrit, Yerinde Çapraz Bağlama, Osteokondral Arayüz Doku Mühendisliği, Tiramin-Konjugesi, Aljinat, Karboksimetilselüloz

Doku mühendisliğindeki son gelişmeler, kıkırdak ve kemik gibi üç boyutlu sentetik doku yapılarının üretimi için büyük bir potansiyel olduğunu göstermiştir. Bununla birlikte, farklı dokular arasında yapısal bütünlüğün sağlanması ve doku arayüzlerinin üretilmesi hala büyük zorluklardır. Bu tezde, aspirasyon tabanlı mikro-kapiler ve yerinde çapraz bağlama biyobasım yöntemi kullanılarak hibrit hidrojel yapılarının üretim yaklaşımı kullanılmıştır. Geliştirilen bu Biyobasım yöntemi ile, farklı hücre yüklü hidrojel biyomürekkepler cam mikro-kapiler'den üç boyutlu (3B) basılarak tasarlanan geometrik yapılar oluşturuldu. Mezenkimal Kök Hücreler (MSC) yüklü aljinat ve karboksimetil selüloz biyomürekkepler hücre biyoaktivitesini ve mekanik özelliklerini geliştirmek için tiramin ile modifiye edildi. Hidrojeller, görünür ışık altında rutenyum (Ru) ve sodyum persülfat (SPS) foto-başlatıcı mekanizma ile yerinde çapraz bağlama yaklaşımı kullanılarak mikro kapiler camda jelleştirilerek ekstrüzyon için hazırlandı. Geliştirilen biyomürekkepler daha sonra aspirasyon-ekstrüzyon mikrokapiler biyobaskı tekniği kullanılarak gradyan kıkırdak-kemik dokusu arayüzü biyobasıldı. 3B biyobasılan yapılar, kondrojenik/osteojenik kültür ortamında üç hafta boyunca inkübe

edildi. 21 günlük inkübasyon ile MSC hücrelerinin farklılaşmasından sonra, histoloji, immünohistokimya ve canlı/ölü testleri yapıldı. Kıkırdak ve kemik oluşumu için yapılan hücre hizalaması ve histolojik değerlendirme sonuçları, mekanik ve kimyasal etkiler ile basılan MSC yapıların kondrojenik ve osteojenik dokulara başarılı bir şekilde farklılaştığını gösterdi.

## ACKNOWLEDGEMENTS

I consider myself extremely fortunate to have graduated from this lovely environment where I was able to grow academically and personally during my master's studies.

Firstly, I would like to express gratitude to my supervisor, Prof. Bahattin Koc, for his supervision and support throughout the process of this thesis. I am also grateful to my jury members, Prof. Sevil Yücel and Asst. Prof. Nur Mustafaoğlu for their interest in my thesis and valuable comments.

In my thesis, I thank every member of the Koç Research Group for the support, especially my late work hour colleague Dr. Çiğdem Bilici for great motivation and Dr. Ferdows Afgah for the valuable information she shared beginning and execution of the studies.

Last but not least, I would like to thank my dear family, who have always believed in me and supported me on this long journey. All my dear friends Gizem Demir, Sevilay Şahin, Ebru Demir, Ahmetcan Kırlıoğlu, Gubse Nur Aydın, Pelin Kanter, and my lovely boyfriend Doruk Arkış, who have always been there to clear my any stupid question marks and to support my mental health.

I appreciate to TUBITAK for providing me with a scholarship and research funding. (Project no: 218S678)

*To my lovely family & friends…*

## TABLE OF CONTENTS

Page

## LIST OF FIGURES

## LIST OF ABBREVIATIONS

| | |
|---|---|
| **2D** | Two Dimensional |
| **3D** | Three Dimensional |
| **Alg** | Alginate |
| **ALP** | Alkaline Phosphatase |
| **ANOVA** | One-Way Analysis Of Variance |
| **ATCC** | American Type Culture Collection |
| **ATR** | Attenuated Total Reflectance |
| **BCA** | Bicinchoninic Acid |
| **BMSCs** | Bone Marrow-Derived Mesenchymal Stromal Cells |
| **BSA** | Bovine Serum Albumin |
| **$CaCl_2$** | Calcium Chloride |
| **CAD** | Computer-Aided Design |
| **CMC** | Carboxymethyl Cellulose |
| **DAPI** | 4′,6-Diamidino-2-Phenylindole |
| **DI** | Distiled Water |
| **DMMB** | 1,9-Dimethyl Methylene Blue |
| **ECM** | Extracellular Matrix |
| **EDC** | 1-Ethyl-3-(3-dimethylaminopropyl) carbodiimide |
| **FA** | Furfurylamine |
| **FBS** | Fetal Bovine Serum |
| **FDA** | Food and Drug Administration |
| **FTIR** | Fourier-transform infrared spectroscopy |
| **GelMA** | Gelatin Methacryloyl |
| **Gtn-HPA** | Gelatin-3-(4-Hydroxyphenyl) Propionic Acid |
| **$H_2O_2$** | Hydrogen Peroxide |
| **HA** | Hyaluronic Acid |
| **HACs** | Human Articular Chondrocytes |
| **HRP** | Horseradish Peroxidase |
| **ID** | Inner Diameter |
| **LAP** | Lithium phenyl-2,4,6-trimethylbenzoylphosphinate |
| **M-PER** | Mammalian Protein Extraction Reagent |
| **MSC** | Mesenchymal Stem Cells |
| **NaCl** | Sodium Chloride |
| **NHS** | N-Hydroxy Succinimide |

| | |
|---|---|
| **OA** | Osteoarthritis |
| **OC** | Osteochondral |
| **OD** | Outer Diameter |
| **PCL** | Polycaprolactone |
| **PDMS** | Poly(dimethylsiloxane) |
| **PEG** | Polyethylene Glycol |
| **PFA** | Paraformaldehyde |
| **PGA** | Polyglycolic acid |
| **PI** | Propidium Iodide |
| **pNPP** | P-Nitrophenyl Phosphate |
| **PVA** | Poly-Vinyl Alcohol |
| **Ru** | Ruthenium |
| **SEM** | Scanning Electron Microscope |
| **sGAG** | Sulfated Glycosaminoglycan |
| **SPS** | Sodium Persulfate |
| **STL** | Stereolithography |
| **Tyr** | Tyramine |
| **UV** | Ultraviolet |

Thesis Structure

This thesis consists of two chapters. Chapter 1 includes 3D bioprint oosteochondral interface (unpublished work ) and Chapter 2 contain works of a published article (Çiğdem Bilici, Asena G Tatar, Efsun Şentürk, Caner Dikyol, Bahattin Koç. Bisulfite-initiated crosslinking of gelatin methacryloyl hydrogels for embedded 3D bioprinting. Biofabrication 2022, 14(2) 025011. https://doi.org/10.1088/1758-5090/ac4dd9)

# Chapter 1

## 1. Introduction

Bioprinting is a rapidly evolving technique in tissue engineering that allows the fabrication of complex and multiphasic structures that could mimic native tissues physiochemically. It enables the precise deposition of various cells in concert with different biomaterials (Aljohani et al., 2018; Huang et al., 2017). Recent advancements demonstrate great potential for manufacturing substrates for soft and hard tissues such as cartilage and bone. These approaches are mostly the use of reinforced hydrogels or scaffolds encapsulated with cells and bioactive molecules (Galarraga et al., 2022; Sheehy et al., 2015) , scaffold free approaches (Athanasiou et al., 2013; Mesallati et al., 2014), and their combination to fabricate multilayered constructs (Shim et al., 2016). In spite of all the progress for regeneration of individual tissues, the fabrication of a hybrid structure for soft to hard cartilage-bone tissue interfaces is still in its infancy. Osteochondral interface is where viscoelastic cartilage meets bone with different physiochemical and mechanical properties. The hierarchical and gradient nature of the interface facilitate its load bearing applications and further assist the he structural functionality in articular joints and the spine (Bicho et al., 2018).

Manufacturing a hybrid structure that can mimic the intricate properties of the interface is a possible approach for the treatment of bone to cartilage tissue injuries (Critchley et al., 2020; Sheehy et al., 2015). A modern technology that has effectively generated continuous gradient hybrid creation of two materials utilizing the aspirated-extruded process may also be assessed for osteochondral tissue (Nadernezhad et al., 2016). Natural hydrogels such as gelatin, hyaluronic acid, and collagen have emerged

promising results for the tissue engineering of osteochondral defects which could stimulate the formation of extracellular matrix (ECM) (Boys et al., 2017). To enhance the mechanical properties of these hydrogels, several strategies including crosslinking mechanism (Homenick et al., 2011; C. R. Lee et al., 2001), reinforcing with stiff materials (Galarraga et al., 2022; Schipani et al., 2020), and increasing crosslinking density (Bensaïd et al., 2003; Yanbin Wu et al., 2009) have been developed. Although the incorporation of reinforcing agents or increasing crosslinking density could hinder cell migration and nutrient flow, as well adverse effect of the degradation products of the stiff polymer materials (I. L. Kim et al., 2011; van Sliedregt et al., 1992).

Crosslinking mechanism is another key factor for a successful fabrication regarding the mechanobiological properties of the fabricated cell-laden hydrogel. Considering that the most common crosslinking methods are using a chemical reagent or photocrosslinking. The latter can be modified for fine tuning of final properties of the hydrogel. Photocrosslinking via visible light has been used recently for the crosslinking of gelatin or GelMA with no negative effects on cell viabilities (Afghah et al., 2022; Lim et al., 2019a, 2020).

Another important aspect of the crosslinking mechanism is the printability and shape fidelity. The visible light crosslinking of gelatin allows the printing at room or body temperature while holding its shape due to physical crosslinking, followed by chemical crosslinking of the bioprinted structure during or directly after printing process.

In this study we modified alginate and carboxymethyl cellulose with tyramine to enhance their bioactivity and mechanical properties and bioprinted MSC-laden structures for the cartilage-bone tissue interface. The overall scheme of the proposed work is given in Figure 1. To address the narrow and fine interface region, we used a glass microcapillary extrusion based bioprinting technique. The biofabricated constructs were co-cultured in chondrogenic/osteogenic culture media for three weeks. Analyses of cartilage and bone formation were conducted based on cell alignment and histological assessment and the results showed that mechanical cues together with chemical cues lead to the differentiation of MSC into chondrogenic and osteogenic tissues. The mechanical properties of the two biomaterials were assessed using compression test. The finding of our study revealed the high resolution of the printing structure with two

distinct regions showing the potential of this approach for the osteochondral tissue interface applications.

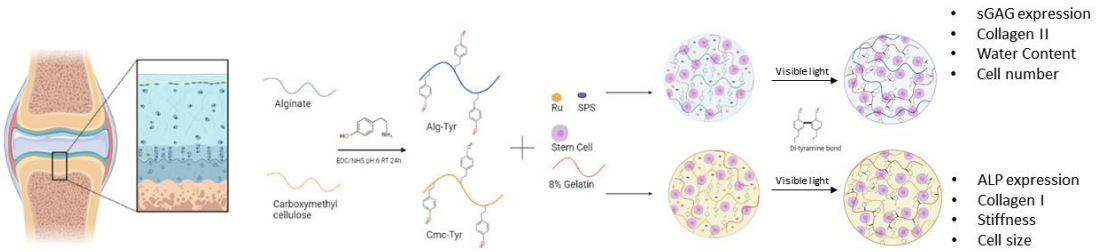


Figure 1: Scheme of the aim of the study

## 1.1. 3D Bioprinting

Bioprinting process is used for fabricating three dimensional (3D) objects by adding biomaterials with the cells layer-by-layer. First, a computer model of the object needs to be sliced into two-dimensional (2D) layers with a specified thickness prior to 3D bioprinting. Based on the calculated paths, these 2D layers are than formed by adding bioinks in a highly reproducible layer-by-layer process (Figure 2).

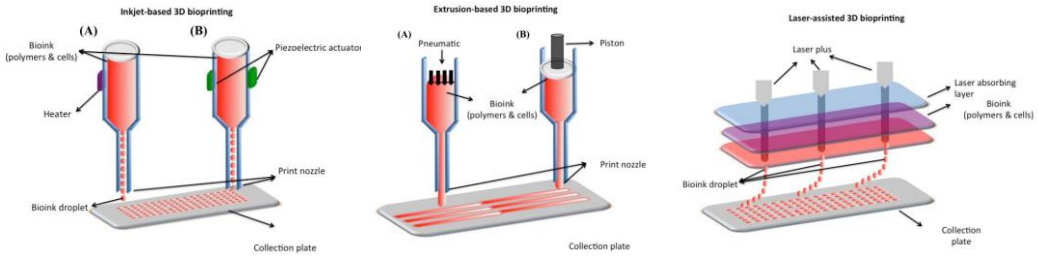


Figure 2: Shematic diagrams of (A) inkjet-based, (B) extrusion-based, (C) laser-assisted bioprinting.
(Liu, Liu, et al., 2018)(Turunen et al., 2018)

Thermal or acoustic force is used to spray liquid droplets onto a substrate to create layer-by-layer structures in inkjet droplet-based bioprinting processes. Bioink droplets are created in the inkjet method by electrically heating the print head or sprayed using an acoustic field. Laser-assisted bioprinting uses laser pulses to induce microbubbles, similar to inkjet printers (Skardal & Atala, 2015). It can create micro cell-laden 3D constructs with polymer viscosities ranging from 1 to 300 mPa/s in high resolution

(Pereira et al., 2017). The high cost of laser-assisted 3D bioprinters is a disadvantage of laser-assisted bioprinting in organ 3D bioprinting. It offers a wide range of applications because to its precise control of deposition, simplicity, and adaptability, including regenerative medicine (Joseph Rey et al., 2021; Sakai et al., 2017).

Stereolithography (STL) is a nozzle-free, solid free-form method that uses a photosensitive macromolecule (or polymer) formulation for 3D bioprinting of organs (Guvendiren et al., 2016). Through the selective photo-initiated curing reaction of a low-molecular-weight prepolymer, additives, and photo-initiators, it is a multi-layer process. The STL printing procedure allows for the addition of a variety of biomaterials (Joseph Rey et al., 2021). In stereolithography techniques used for 3D bioprinting, the ability to create and detail the structure at high speed is an advantage, but the high cost of the equipment used in this printing and the cytotoxicity of photo-initiators are some of the disadvantages (Liu, Liu, et al., 2018). Among these printing processes, extrusion-based bioprinting has been mostly utilized for manufacturing 3D cell-laden constructs. More details of extrusion-based bioprinting are given in the next section.

## 1.2. Extrusion-based Bioprinting

Extrusion-based bioprinters are commonly built with a three-axis (x, y, z) automated extrusion mechanism and a fluid-gel dispensing nozzle ased on the intended coordinates (or direct from the head) (Guvendiren et al., 2016; Skardal & Atala, 2015). During extrusion procedures, cell-laden bioinks are deposited in cylindrical filaments based on a computer-controlled instructions calculated from a CAD model of the object. It is the only technique able to create large-scale cell-loaded structures in both controlled micro- and macrophysiological conditions (Pedde et al., 2017). A single-nozzle 3D bioprinter or a multi-nozzle 3D bioprinter can be used to construct heterogeneous tissues and organs (Jungst et al., 2016).

Two important elements that affect the final 3D constructions in extrusion-based bioprinting are 3D printers and biocompatible polymers. The resolution, form, and quality of the 3D structures are all dependent on how easily the polymeric solutions or hydrogels can be printed (X. Wang, 2019). In addition to polymeric solutions or

hydrogels, natural extracellular matrices (ECMs) and cell aggregates can be employed as bioinks (Toprakhisar et al., 2018). Large 3D structures, high cell densities, and relative rapid printing processes are a few advantages of extrusion-based techniques for tissue 3D bioprinting.

### *1.2.1. Microextrusion Bioprinting*

Microextrusion is the most promising form of extrusion-based bioprinting, in which the bioink is dispersed from the nozzle using mechanical or pneumatic processes to create 3D tissue structures (Bishop et al., 2017; Ouyang, 2019). Unlike inkjet bioprinters, micro-extrusion bioprinters can print a variety of materials with varying viscosities, allowing them to work with cell-laden biomaterials (Ozbolat & Hospodiuk, 2016).

Additional factors such as printing speed, dispensing pressure or mechanical force, and distance must be considered in this technique. These parameters, which differ for the targeted tissue and used material, are critical for cell viability and must be optimized (Skardal & Atala, 2015). Bishop et al. discovered that the viability of bovine aortic endothelial cells enclosed in collagen for 250 and 90 micron diameter nozzles was 86 % and 46 %, respectively, when investigating the importance of printing parameters (Bishop et al., 2017).

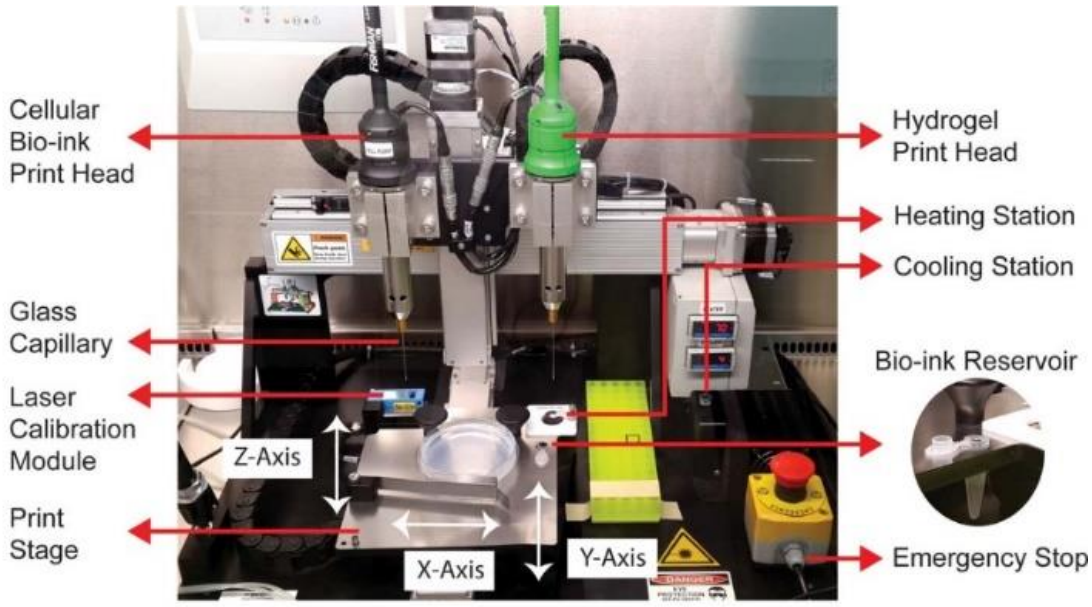


Figure 3: The image of Bioprinter (Organova) platform describing its parts.
(Ozler et al., 2017)

As shown in Figure 3, the bioprinter used in this study is a modified NovoGen MMX (Organovo), which is an automated platform designed to fabricate 3D tissue engineered cell constructs with precision X-Y-Z motion systems. It also has two deposition heads with 450/500 μm inner/outer diameter dispensing glass capillaries. The motion system's positional repeatability is approximately 10 μm, and the positional accuracy between the two deposition heads is maintained using a laser-based calibration system. The bioprinter has heating and cooling chambers with temperature ranging from room temperature to 95°C and 4°C to room temperature, respectively. The print stage can be designed to fit standard 100- or 150-mm petri dishes.

### 1.3. Printing Characteristics

A key concept in describing the printability of bioinks and their form after deposition is called shape fidelity. Bioinks with poor form integrity may have extrusion lines that are overly broad and have highly constrained heights. Extrusion lines are rotated 90 degrees every other layer for at least two layers in the crosshatch design, which is the most often employed for bioprinting (Gillispie et al., 2020). The printer parameters must be adjusted when checking the regularity of the extruded structure and shape conformance

when extruding the continuous filament (Figure 4). The printing pressure, nozzle diameter and speed, as well as the distance between the nozzle tip and the substrate are all important parameters for the shape fidelity. A high shape fidelity also requires the ability to print structures with longitudinal porosity and preventing filament collapse along the axial direction. The bioprinting process causes a deposited bioink strand to deform since bioinks are frequently viscoelastic and mechanically soft. Particularly, the viscoelastic behavior of the soft material can result in the hanging filaments dropping or collapsing (Gao et al., 2018). The two main reasons of these phenomena are gravity, which results in an overall loss of structure due to compression or drooping, and surface tension, which leads filaments to adopt shapes that reduce surface area (Cai et al., 2021). In assessing bioink shape fidelity, two context  quantitative tests due to filament deformation after printing are characterized in this technical note: (i) filament collapse, which measures the deformation and collapse of a suspended filament; and (ii) filament fusion, which measures the determination of the printed filaments in the x-y plane (Ribeiro et al., 2018).

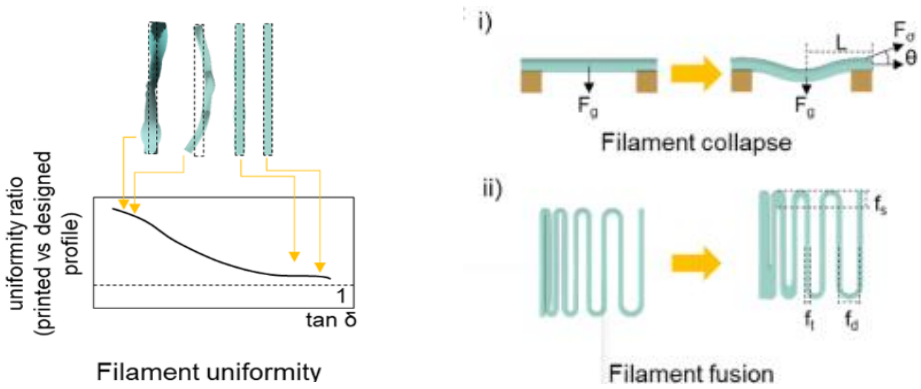


Figure 4: Drawing of single fiber printing, which indicates filament uniformity and shape fidelity which consists filament fusion and collapse. (Schwab et al., 2020)

## 1.4. Photo-Induced Extrusion Bioprinting Methods

The form precision of the print structure and the location of the optical device source are critical in bioprinting processes employing photocrosslinkable ink. The location and timing of these operations in the printing procedure may be altered to control the chemistry of this crosslinking reaction. Photo-crosslinking could be applied before (pre-crosslink), after (post-crosslink), or during (in-situ-crosslink) extrusion, as shown in Fig. 5 (Ouyang et al., 2017a).

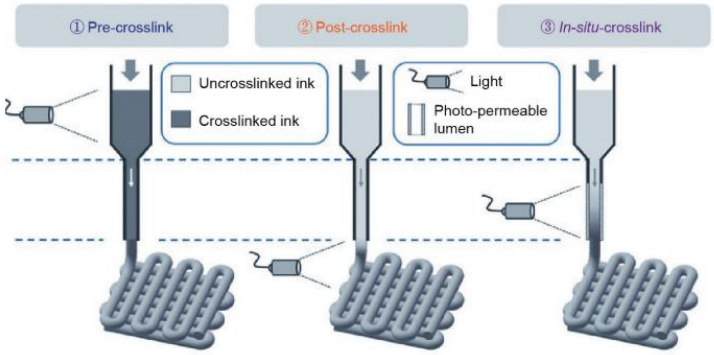


Figure 5: Schematic illustration of extrusion-based bioprinting types (Z. Zheng et al., 2021).

Because all of these crosslinking techniques must maintain the original shape after extruding the material, they must also be resolved. To overcome these problems, photocrosslinking can be recommended just before extrusion rather than after (Z. Zheng et al., 2021). Using a light-permeable microcapillary glass as a crosslinking nozzle for the proposed in-situ crosslink made the hydrogel suitable for gelation before deposition. This *in situ* crosslinking approach enables stable hydrogel crosslinkers to be readily extruded on a variety of hydrogel types while lowering shear stresses that would otherwise limit cell viability. This technology has the benefits of i) not needing copolymerization or viscosity manipulation, (ii) can be used for a diverse photocrosslinkable hydrogel compositions, (iii) permitting to embed live cells, and (iv) allowing to print heterogeneous and complex structures (Lim et al., 2016). The crosslinking density of the ink is determined by the length of the capillary exposed to the light source including the ink feed rate. Using a light-permeable microcapillary glass as a crosslinking nozzle for the proposed in-situ crosslink made the hydrogel suitable for gelation before deposition. This *in situ* crosslinking approach enables stable hydrogel crosslinkers to be readily extruded on a variety of hydrogel types while lowering shear stresses that would otherwise limit cell viability. It was also

demonstrated that this technology may be used to print bioinks with viscoelastic properties that cannot be produced using traditional extrusion-based technologies (Lim et al., 2016).

The required properties of the glass micro-capillaries are its light permeability and smooth resistance. Microcapillary glass (micropipette tubing) is constructed from borosilicate glass tubes with inner diameters (ID) ranging from 0.5 to 1.56 mm and base outer diameters (OD) ranging from 1, 1.2, 1.5, and 2.0 mm. Sigmacote is applied to the inner surface of a glass capillary as a pre-treatment to make it hydrophilic and reduce internal gel resistance. The material unit in the Organovo machine is made in accordance with micro capillary glasses with specific inner diameters by using stainless steel wires as pistons in the print heads that extudes the material. Furthermore, by keeping the piston vertically fixed, this mechanical head prevents any bending or distortion and ensures the protection of the structure and microcapillary glass during biorinting process.

## 1.5. Crosslinking Methods for 3D Bioprinting

Crosslinking is an important mechanism that influences the physicochemical characteristics and biological activity of bioprinted objects. Crosslinking of hydrogel bioinks (cell-laden inks) can be accomplished using a range of processes, including chemical, physical, enzymatic, or a combination of these, depending on the polymeric backbone and functional groups (GhavamiNejad et al., 2020).

### *1.5.1. Physical Crosslinking*

Physical crosslinking types in bioprinting are generally mechanically weaker than chemical crosslinking types, as they rely on hydrophobic interactions, electrostatic attraction, or h-bond formations (Trabbic-Carlson et al., 2003). Gelation in crosslink

types based on ionic interaction, which supports a cell-friendly environment is achieved by adding multivalent cations to the polymer solution (Bialik-Wąs et al., 2021). Crosslinking sodium alginate with $Ca^{2+}$ ions is a well-known example in 3D bioprinting (Axpe & Oyen, 2016). However, it has certain drawbacks, including as limited mechanical strength, poor layering, and the possibility of metal ions leaking into the body after implantation (GhavamiNejad et al., 2020).

### *1.5.2. Chemical Crosslinking*

Covalent connections between polymeric chains generate a chemically crosslinked hydrogel network. This is typically accomplished by the addition of chemical crosslinkers (such as sodium persulphate or benzoyl peroxide) or through various chemical reactions such as Schiff base chemistry, azide-alkyne cycloaddition, hydrazide-aldehyde coupling, thiolene coupling, enzymatic crosslinking, or by the use of various ultraviolet (UV), visible, or near-infrared lights (Hammer et al., 2021). Although these hydrogels are normally robust enough to maintain the required form stability, crosslinking kinetics must be carefully tuned to avoid printer nozzle clogging (GhavamiNejad et al., 2020).

Enzymes can also be utilized as catalysts to aid in the production of covalent bonds between protein-based polymers. Enzymatic crosslinking is an attractive method for use in 3D bioprinting since the enzymatic reactions are moderated, which may prevent cell death (Moreira Teixeira et al., 2012). On the other hand, 3D bioprinting has seldom ever employed these crosslinking methods alone or in combination.

During 3D printing, several chemical crosslinking processes may also be thermally activated and applied to polymers, maintaining the heating and cooling cycle. Despite being the most straightforward crosslinking approach, it has certain disadvantages for 3D printing, including a longer gelation time than the alternatives and an unregulated crosslinking degree (Ashammakhi et al., 2018; Ouyang et al., 2017b)

### *1.5.3. Photocrosslink*

Photocrosslinking has special relevance for 3D printing applications and has been favored by the 3D printing industry due to the rapid and on-demand polymerization reaction. A number of 3D bioprinting techniques, including as stereolithography (Castro et al., 2015), digital light processing (Mao et al., 2020), and volumetric bioprinting (Yun Wu et al., 2018), have been used to create the 3D structure of photocurable bioinks. All of these methods allow for the crosslinking of photocurable bioinks by redox-based processes, chain-growth techniques, or step-growth techniques in the existence of photoinitiators.

Previous biofabrication approaches utilized the UV light-curing Irgacure 2959 photoinitiator, but its concentrations are restricted due to cell toxicity (Nieto et al., 2020). Several research have found the appropriate irradiation period that allows for cell viability and functioning preservation (Kolesky et al., 2014). At various wavelengths, different photoinitiators are utilized for photocrosslink processes. Several UV-A or visible light sensitive photoinitiators have been evaluated for biofabrication purposes, including lithium phenyl-2,4,6-trimethylbenzoylphosphinate (LAP) (Lim et al., 2019a), and ruthenium (Ru)/sodium persulfate (SPS) (Ru/SPS) (Rapp et al., 2018). Another strategy to decrease the possible dangers of UV exposure is to use lower energy (visible) light from one of these wavelengths.

#### *i. Visible light initiators with Ru/SPS*

Photoinitiators employed under visible light are classified as either free radicals or cationics, nevertheless since protonic acid is generated as a byproduct in cationic research, it cannot be preferred in biomedical applications (Nieto et al., 2020). Therefore, free radical photoinitiators are the primary initiators in the formation of visible light crosslinkable hydrogels. Type I free radical photoinitiators (one-component pyrolysis) and type II photoinitiators (photosensitizer/co-initiator) are the two types (Gonzalez-Fernandez et al., 2020). Ru/SPS, or ruthenium complex with sodium persulfate (SPS), is a visible light initiation method that is particularly interesting in the

biofabrication technology and also provides in unique compressive performance of hydrogels (Rapp et al., 2018)(Lim et al., 2019b)(Lim et al., 2016). After irradiation, Ru2+ photoexcites to Ru3+, and Ru3+ donates electrons to SPS, which dissociates into sulfate anions and radicals as shown in Figure 6. (Van Hoorick et al., 2019). Oxygen inhibition during polymerization can be reduced by Ru/SPS, which improves the fidelity of 3D bioprinting (Lim et al., 2016). Since Ru/SPS has a high molar absorptivity, it can be considered as a very effective photoinitiator (GhavamiNejad et al., 2020). Oxygen inhibition has a direct effect on the photo-crosslinked hydrogel structure and the printing accuracy of 3D bioprinting, as free radicals interact with oxygen which increases the fidelity of the structure and can be reduced by Ru/SPS (H. Kim et al., 2021).

Notably, visible light crosslinking of GelMA in the presence of Ru/SPS increased the survival of human articular chondrocytes (HACs) and bone marrow-derived mesenchymal stromal cells (BMSCs) more than UV crosslinking in the presence of Irgacure 2959 (Lim et al., 2019a). Because of the benefits of visible light crosslinking, it will become a more cytocompatible strategy and will aid in the expansion of biofabrication by eliminating potentially damaging irradiation procedures.

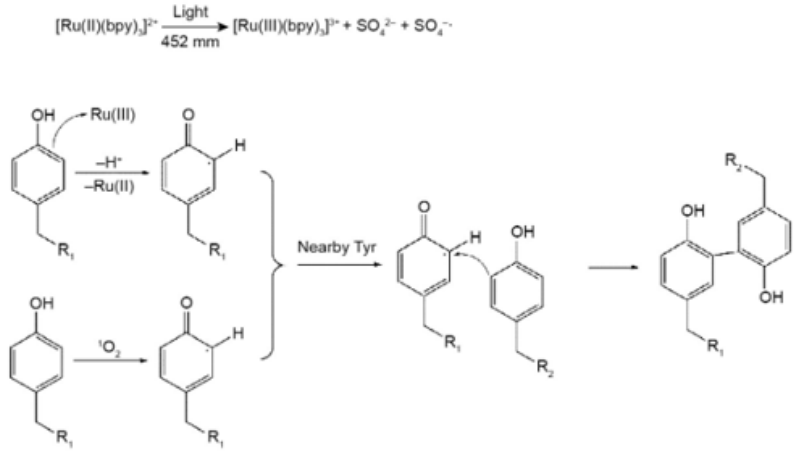


Figure 2: The mechanism of photo coupling reaction of Ru/SPS (Zheng et al., 2021).

Recently, hydrogel structures consisting of GelMA (Lim et al., 2016), gelatin (S. M. Wei et al., 2020), and hyaluronic acid (HA) polymers (Sakai et al., 2018) have been produced via the bioprinting method combined with Ru/SPS mechanism. In bioprinting techniques, phenolic-substituted derivatives polymers such as Alginate-Tyr

(Khanmohammadi et al., 2019), Gelatin-Tyr (S. M. Wei et al., 2020), GelMA-Tyr (Lim et al., 2020), and poly(-glutamic acid) (H. C. Kim et al., 2021) are also frequently examined under the Ru/SPS crosslinking method due to their rapid crosslinking and control of polymer viscosity with this method.

## 1.6. Bioinks Components

The preference of biomaterials is an important step in applying the complex biophysical and biochemical structure of tissue-interfaces (Skardal & Atala, 2015). These materials must not only supply structural cues but also match other criteria such as printability, biocompatibility, and biodegradability. A wide range of polymers have been evaluated for biocompatibility and printability or have been modified to improve those properties and provide required biological, chemical, and mechanical elements similar to natural tissues (Guvendiren et al., 2016). Modifications are also made to their viscoelastic properties to make them suitable for printing. When the modification process is simplified, it simply involves mixing the modifiers in the polymer and chemical bonding prior to printing under specific conditions such as temperature and pH.

Since most hydrogels are made of polymers (such as polysaccharides like alginate (Alg) and carboxymethyl cellulose (Cmc), which have a good biocompatibility towards many cells, they are desirable for cell encapsulation. By coming into close touch with the cells and replicating the environment of the natural ECM, they promote structural integrity and modulate the chemical and physical characteristics of bioinks (Markstedt et al., 2015; Yun Wu et al., 2018)

### *1.6.1. Gelatin*

Gelatin is a kind of partially hydrolyzed collagen that is obtained from various animal tissues, including fish and bovine tendon. Gelatin, in contrast to its progenitor collagen, is a typical linear natural polymer that responds to heat and is great in terms of water solubility, biocompatibility, biodegradability, and 3D printability (Xiao et al., 2011).

Proteoglycans or glycoproteins, which are the building blocks of gelatin-based bioinks, are similar to ECMs in that they support cell adhesion, viability, proliferation, and differentiation. This means that 3D printed constructs can be designed to have similar water content and elastic modulus to those of soft organs with excellent in vitro cell and in vivo tissue properties (X. Wang, 2019).

Due to the inability of gelatin to create crosslinked stable hydrogels at physiological temperatures, 3D printed constructions rupture when put in culture media at physiological temperatures, such as 37 °C. Through several extrusion-based 3D bioprinting models, other natural polymers such alginate, fibrin, chitosan, hyaluronate, carboxymethyl cellulose, and fibrin added as additives to the gelatin solution have been investigated (Al-Abboodi et al., 2014; Liu, Chen, et al., 2018; X. Wang et al., 2013).The production of covalently cross-linked hydrogels, known as unsaturated methacrylamide groups, GelMA, (gelatin methacrylamide, gelatin methacryloyl, gelatin methacrylate) is another common gelatin functionalization study (Yue et al., 2015; Lee et al., 2016) .

3D bioprinted scaffold from fibroin and gelatin has been effectively employed for in vitro chondrocyte culture and in vivo cartilage injury healing in gelatin samples in bone and cartilage tissue-specific research (Shi et al., 2017). In vivo cell proliferation has been reported when the stem cell is a bioprinted scaffold made of MSC-loaded cellulose and alginate hydrogels (Haldar et al., 2019).

### *1.6.2. Alginate*

Alginate is an anionic polysaccharide of mannuronic acid and guluronic acid obtained from seaweeds and algae. It forms a stiff hydrogel upon addition of calcium ions due to sodium-calcium ion exchange reactions (Giuseppe et al., 2018). It has been used as a promising hydrogel for tissue engineering due to its inert nature. Alginate is mainly utilized by physically mixing or chemically modifying with other biomaterials such as gelatin, fibrin, poly-vinyl alcohol (PVA), and HAp to provide ECM molecular cues, that would be more appropriate for cell-ECM interaction, cell attachment and

differentiation, and multicomponent environment (Axpe & Oyen, 2016; Giuseppe et al., 2018; Jang et al., 2019; H. C. Kim et al., 2021).

The low mechanical strength of alginate can be improved by employing a physical and chemical crosslinking strategy that exhibits the physical characteristics required for the use of cartilage tissue. The literature further demonstrates that alginate has been thoroughly examined and studied for uses in cartilage regeneration (Farokhi et al., 2020). Kim et al. demonstrated high printability and structural integrity that aids in vitro chondrogenic differentiation while forming a multilayered composite scaffold with strong mechanics and excellent cell survival by coating an alginate-based bio-ink on the PCL surface. (J. E. Kim et al., 2016).

### *1.6.3. Carboxymethyl cellulose*

Carboxymethyl cellulose (Cmc) is a good potential polysaccharide candidate for tissue engineering (Chang et al., 2010). Cmc has been commercially produced since the early 1920s and has been widely used as an FDA-approved material in tissue engineering, drug delivery, and dentistry due to its water solubility, low cost, and biodegradability (Sakai et al., 2009). Similar to alginate (Uludag et al., 2000), it can be used as an anti-adhesive coating for biomaterials, such as the anti-adhesive coating of cell-enclosing microcapsules for cell therapy. (Priya et al., 2021) (Zhong et al., 2019)

In biofabrication studies, it is usually prepared as a hybrid hydrogel with other biomaterials such as alginate and gelatin to achieve the desired pore size and geometric structure (Habib et al., 2018). The hybrid hydrogel enables the achievement of physical gelation characteristics and solidified filament morphology after extrusion to support the successive layers (Zhong et al., 2019). An example of these hybrid biomaterials developed for bone applications is a 3D injectable hydrogel-bioceramic composite containing fish scale and gelatin-3-(4-hydroxyphenyl) propionic acid (Gtn-HPA) and carboxymethyl cellulose-tyramine (Cmc-Tyr) derived calcium phosphate (CaP) (Chun et al., 2016) (He et al., 2020). Furthermore, a composite tripolymeric bioink composed of gelatin, carboxymethyl cellulose (Cmc), and alginate was optimized and

characterized for printability, structural, biomechanical, and biofunctional properties. The same bioink was also used for direct 3D printing of a hierarchical patient-specific customized human meniscal scaffold (Gopal & Selvakumar, 2022).

### *1.6.4. Tyramine Conjugation-Modification*

Tyramine is a biogenic ammonium found in both plants and animals. It has a phenolic ingredient and an amino group at the end, which makes it a good binding site for the carboxyl groups of polymers. In previous studies, tyramine conjugation was used for a wide range of natural polymers such as hyaluronic acid (F. Lee et al., 2008), poly(aspartic acid) (Hou et al., 2015), alginate (Hou et al., 2015), polyethylene glycol (PEG) (Hong et al., 2019), carboxylmethyl cellulose (Sakai et al., 2009) and gelatin (Ahmadian et al., 2021) to induce an enzyme using horseradish peroxidase (HRP) and hydrogen peroxide ($H_2O_2$) or EDC/NHS mechanism. In addition, an example of tyramine enzymatic crosslink used in dual crosslink mechanisms is also available in the literature as using furfurylamine and tyramine-modified PGA (PGA–Fa–Tyr) synthesis (M. Wei et al., 2021).

The short gelling time, programmable viscosity and controlled solidification of tyramine conjugates provide improved printability and superior performance (Hong et al., 2019; F. Lee et al., 2008). It offers the possibility for bioink ideal for 3D printing, such as injected hydrogels and cell encapsulations, in addition to the characteristics of these physiologically sensitive systems. Wang colleagues reported a newly developed Gtn hydrogel system with a wider range of stiffness control using Gtn-HPA-tyramine (Gtn-HPA-Tyr) conjugates to stimulate osteogenic differentiation of human mesenchymal stem cells (hMSCs) cultured on the hydrogel(L. S. Wang et al., 2012).

## 1.7. Osteochondral Tissue

The bone-cartilage interface contributes to the osteochondral (OC) entity's structural functioning. This structure has a thickness of 100-200 mm and is made up of four

interrelated constructions: hyaline cartilage, a thin layer of calcified cartilage, subchondral and cancellous bone (Ganesh et al., 2015; Hoemann et al., 2012). Chondrocytes, hypertrophic chondrocytes, and osteoblasts are among the cells engaged in the organized composition of these continuous sections (Khanarian et al., 2014; Zhang et al., 2020). Changes in the organization and nature of the bone-cartilage interface cause disruptions in joint integrity and, as a result, loss of functionality, resulting in OC deficiencies and injuries (Kazemi & Williams, 2021). Significant damage to both articular cartilage and subchondral bone that have a restricted ability to heal are referred to as these types of deformities.

Osteoarthritis (OA) is one of the most debilitating OC related degenerative diseases (Bicho et al., 2018; S. R. Goldring & Goldring, 2016). OA is a degenerative condition affecting the entire joint, not just a surface lesion. The breakdown of joint cartilage connection, synovial inflammation, subchondral bone abnormalities, as well as ligaments, muscles, and neurological tissues, all play a role in the disease's complex initiation and development (M. B. Goldring & Cartilage, 2007). Cracks and microcracks occur along the complex tissue interface structure, and mediators created between the cartilage and subchondral bone penetrate to the neighboring tissues (Findlay & Kuliwaba, 2016). Reduction of glycosaminoglycan (GAG) content altered load patterns, and loss of collagen integrity in the tissue's matrix all contribute to a reduction in mechanical stiffness (Figure 7). Therapies for osteoarthritis (OA) primarily seek to relieve pain (S. R. Goldring & Goldring, 2016).

One of the biggest challenges in this field is fabrication of anatomically accurate OC structures (Yuan et al., 2014). Maintaining molecular communication between tissue layers, incorporating the chondral-osseous interface, and replicating each matrix composition are all extremely challenging and are major therapy barriers (Oliveira Silva et al., 2020).

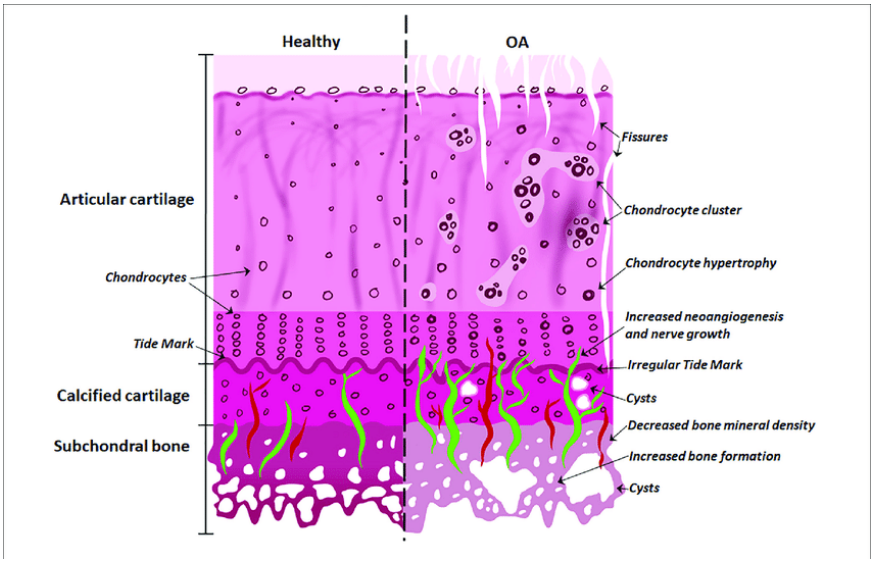


Figure 3: Differences between normal and osteoarthritic osteochondral tissues (Oliveira Silva et al., 2020).

Tissue engineering of soft and hard tissues has become one of the most frequently used methods for cartilage and bone tissue repair (Cui et al., 2012). Although hard bone tissue and soft cartilage tissue have very different properties, they are both important components of the skeletal system overall (Hoemann et al., 2012). The biochemical composition, structure, and mechanical properties of natural OC tissue exhibit a gradient transition from the surface of the cartilage to the subchondral bone. To closely mimic the gradient transition of OC tissue, the cell type (Saghati et al., 2021) (Ahearne & Kelly, 2013), growth factor (M. B. Goldring & Cartilage, 2007), biofabrication material (Dhawan et al., 2019), scaffold structure (Karageorgiou & Kaplan, 2005), mechanical properties (Chen et al., 2011), and culture conditions must also exhibit a gradient transition (Zhang et al., 2020).

With limited methodologies, gradients in the OC interface have been explored. These characteristics complicate the fabrication of scaffolds that successfully mimic the structural and mechanical characteristics of the targeted tissue (Gadjanski & Vunjak-Novakovic, 2015). Using 3D bioprinting methods to achieve the pore structure of the gradient biofabrication with appropriate mechanical and tribological qualities for OC tissue repair is enabled (Karageorgiou & Kaplan, 2005).

### *1.7.1. 3D Hybrid Printed Structure for Osteochondral Tissue*

Hydrogel 3D printing has showed considerable promise for deposition tailored biofabrication in cartilage and bone tissue engineering. An optimal hydrogel matrix for bone and cartilage engineering should encourage cell growth/proliferation, preserve chondrocyte/osteoblast morphologies, and stimulate chondrogenic/osteogenic differentiation of stem cells for osteochondral interface (Daly et al., 2017). The type and number of bioprinted cells are critical factors in bioprinter culture. Furthermore, the manufacture of the spatial differences found in osteochondral tissue is made possible by the capacity to accurately manipulate the patterning of cells and biological components (Li et al., 2021). Cell-cell interactions may be effectively promoted with the support of bioprinted structures, which is essential for creating hybrid tissues (Zhang et al., 2020). By creating a framework that encourages fusion between the chondral and osseous portions for the repair of osteochondral defects can be possible with the application of 3D printing (Nguyen et al., 2017). Bioprinting is therefore useful in the context of osteochondral tissue, where the mechanical and compositional parameters diverge for cartilage and bone tissues (Daskalakis et al., 2020).

In 3D printed constructs for osteochondral tissue regeneration, separate bioink formulations are often employed for the cartilage zone and the subchondral bone (Dhawan et al., 2019). In the created structures, the rates of degeneration and creation should be proportionate such that the manufactured material can collapse under tissue stress and destroy the interface. Rigid and hydrophobic materials were used to restore bone and cartilage, whereas softer materials were chosen based on the mechanical and physical properties of the native tissue (Chen et al., 2011). Fedorovicj et al. made previous attempts by encapsulating human chondrocytes and osteogenic progenitors in alginate hydrogel and biofabricating 3D scaffolds with separate components including both cell types (Fedorovich et al., 2012). The hybrid gradient biofabricated structure has the capacity to produce a successful transition between cartilage and bone; furthermore, it can prevent interface uncertainty and better match the composition of the OC tissue (Jiang et al., 2010). Compared to distinct gradient scaffolds, the continuous gradient scaffold has the capacity to generate a smooth transition between the cartilage and bone

components, decreasing displacement portions at the interface (Zhang et al., 2020). Reconstructing the osteochondral interface, the subchondral bone structure, and the zonal organization of the cartilage are essential for successful regeneration of the OC interface (Chen et al., 2011).

# 1. Materials and Method

## 2.1. Materials

Sodium Alginate, Tyramine, Gelatin (Bovine skin, Type B), and 1,9-dimethyl methylene blue (DMMB) were purchased from Sigma Aldrich. Carboxymethylcellulose was obtained from Balmumcu Kimya. Trypsin-EDTA solution, Penicillin-Streptomycin, paraformaldehyde (PFA), sodium chloride (NaCl), Glycine, Alizarin Red S, chondroitin-4-sulfate, Alcian Blue 8GX were purchased from Sigma. Human bone marrow-derived mesenchymal stem cells (MSC), MSC Basal Medium and Supplement Kit, and Osteocyte Differentiation Tool were purchased from ATCC. StemPro™ Chondrogenesis/osteogenesis Basal Medium, StemPro™ Chondrogenesis Differentiation Tool, M-PER ™ Mammalian Protein Extraction Reagent, Tris/HCl, BCA Protein test kit BSA were purchased from Thermofisher Scientific. Fetal Bovine Serum FBS was provided by Pan Biotech. Triton X-100 was obtained from AppliChem. Calcein-AM (green fluorescence) was purchased from Life technologies. Acetic acid was provided by Merck. Calcein-AM and propidium iodide was obtained from Invitrogen. Alexa Fluor® 546 Phalloidin and 4′,6-diamidino-2-phenylindole (DAPI) were purchased from Life Technologies and Thermo Fisher, respectively. p-nitrophenyl phosphate (pNPP) liquid substrate system was provided by Sigma. ProteinaseK and

TRIzol Reagent were purchased from Ambion. Cryostor cell cryopreservation media was obtained from Sigma Aldrich.

## 2.2. Synthesis of tyramine-modified alginic acid and carboxymethylcellulose

Alg-Tyr conjugates were produced by modifying alginic acid with tyramine using EDC/NHS catalysis.1.08 g Alg was dissolved in 100 mL of distilled water in a brief. After adding EDC and NHS (both 5 mmol), and 2.5 mM Tyr in that order, the solution was purged with nitrogen and stirred at room temperature overnight in Figure 8 (A). The solutions were lyophilized after being dialyzed against DI water for three days as shown in Figure 8 (B).

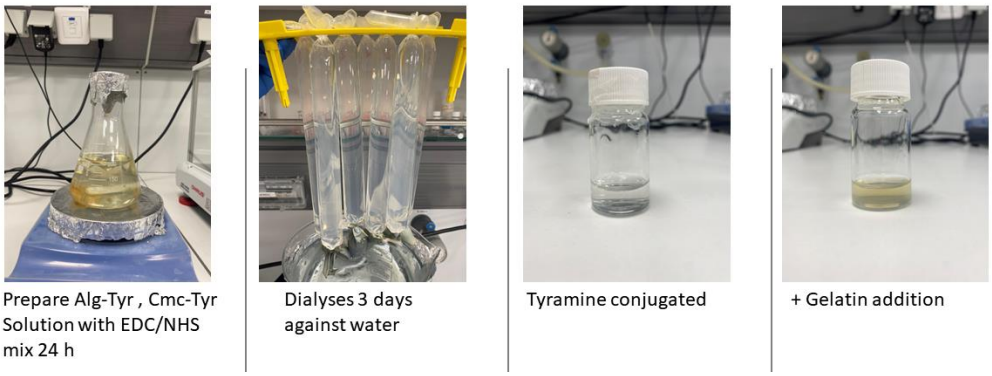


Figure 4: Synthesis steps of Tyramine conjugate

The same synthesis method was applied to the Alg-Tyr conjugate for the synthesis of the Cmc-Tyr conjugate. 1 g of sodium carboxymethyl cellulose was dissolved in 100 ml of DI water and EDC and NHS (both 5 mmol) were added and then 6 mM Tyr. The solution was purged with nitrogen and stirred allowing reaction overnight. Before lyophilization, the solution was dialyzed against 0.1M NaCl, 25% ethanol, and lastly DI water for 2 days each (Chun et al., 2016).

## 2.3. Casting of photocrosslinked Alg-tyr-gel, Cmc-tyr-gel hydrogels

The casting of Alg-Tyr-Gel and Cmc-Tyr-Gel hydrogels produced with Ru/SPS combination under visible light for mechanical properties. Briefly, synthesized Alg-Tyr and Cmc-Tyr solutions prepared 0.5% and 0.05% in PBS respectively, and %8 Gelatin final concentration was added and stirred until homogenization at 37 C. For provided visible-light cross-linking 0.1/1 Ru/SPS (mM/mM) was added, and the solution was aspirated into a 2 ml syringe. After solutions were exposed to visible light for 10 mins 400 $mW/cm^2$, then hydrogels were sliced into 10 mm lengths.

However, for cell differentiation tests, the Alg-Tyr, Cmc-Tyr, Gelatin, and Ru/SPS concentrations remained unchanged. 3x106 cells/ml hMSCs for bone tissue differentiation and $1x10^7$ cells/ml hMSCs for cartilage tissue differentiation were embedded in the Cmc-Tyr-Gel and Alg-Tyr-Gel hydrogels, respectively. The solution was poured into a 48-well plate, and visible light at 400 mW/cm2 was applied for 1 minute.

## 2.4. 3D Bioprinting & Printing of Alg-Tyr-Gel, Cmc-Tyr-Gel Hydrogels

NovoGen MMX (Organovo) bioprinter was used for creating an interface area of the osteochondral and printed structure which had a 7.5 mm length and 500 μm diameter microcapillary glass and there is a plunger inside that allows it to aspirate and extrude the biomaterial with up and down displacement. A tissue interface area is created by extruding a specified length of previously aspirated ink inside the reservoir of the next ink just before beginning the next aspiration.

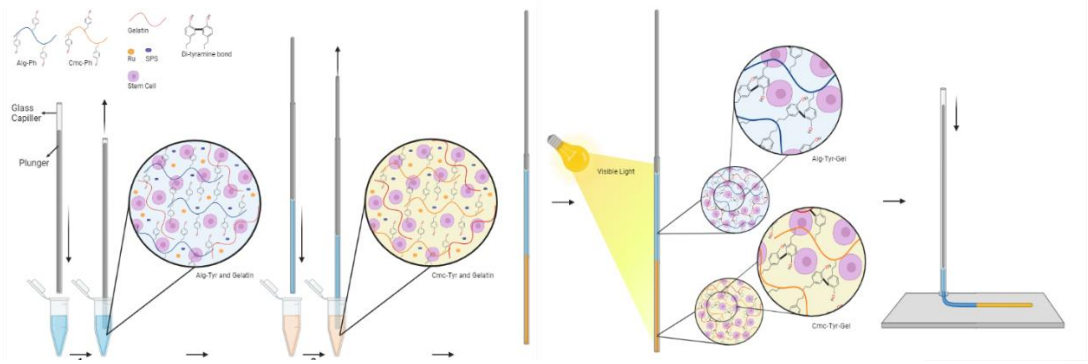


Figure 5: A schematic representation of the bioprinting procedure

Alg-Tyr-Gel and Cmc-Tyr-Gel bioink solutions prepared in separate reservoirs are kept at 37°C in the bioprinter's heater section. Figure 9 shows a schematic representation of the bioprinting procedure. The first material to form the interface was aspirated into the microcapillary glass capillary as a result of the plunger's upward movement (2 mm/s, 25 mm) in the microcapillary glass entering the Alg-Tyr-Gel bioink reservoir to be used for cartilage tissue differentiation. The first bioink containing microcapillary glass is then moved into the Cmc-Tyr-Gel ink reservoir used for bone tissue differentiation. First, the plunger extrudes the first bioink (2 mm/min, 0.5 mm) while microcapillary glass is presented in the second bioink and then aspirates the second bioink, Cmc-Tyr-Gel, via the plunger's upward motion (2 mm/min, 25 mm), lead to the formation of two gradient ink mixtures. When the bioprint head reaches the print area, the visible light source is initiated, and a mixture of two bioink gels in microcapillary glass and materials is printed by starting to move the plunger towards the print stage. When the microcapillary glass tip reaches the printing area, the visible light source is initiated and the material is exposed to light for 15 seconds. After the gelation in the microcapillary glass is complete, the piston begins to move toward the platform, and the printing is completed as adjacent single fibers with an offset of 0.1 µm on the Z-axis about 0.4 µm above the platform with a 2 mm/min feed rate.

The printed structures were fabricated as follows: the material was aspirated with a plunger for all grid, round, and star shapes with a diameter of 500 µm microcapillary glass and then exposed to light for 15 seconds to achieve *in situ* gelations. Aspiration and dispensation speeds were set to 2 mm/min. 2-layer grid structure was printed at the size of 2 x 2 mm with a Z-axis difference of 400 µm. The diameter of the circular structure is 6 mm, designed as 2 extrusions side by side. Star shape model has arms with

a length of 5mm and printed to show sharp corners. Print fidelity was demonstrated by printing single fiber with various feature dimensions from 8 mm to 1 mm, and for filament collapse assay by printing single fiber on PDMS with spaces of 2 mm, 4 mm, and 16 mm.

To investigate interface structures, a mixture of two different fluorescent colors (blue and red) was added to the two inks and were printed with the bioprinting method without cells. Briefly, after the first ink aspiration, the plunger has an upward movement length of 0.5 mm to create a gradient interface mixture and for a sharp distinction between two materials without any plunger motion in the second reservoir. Single and multilayered filaments were printed with 2 mm/min feed speed and images of the inks were taken in a microcapillary glass, as a single fiber and multi-fiber printed under UV light.

## 2.5. The Morphological Characterization of Hydrogel Structures

The morphological structures of the lyophilized gel samples were characterized using JEOL JSM 6010 scanning electron microscope (SEM). The samples were coated with Au-Pd under vacuum and scanned at 3 kV accelerating voltage and a working distance of less than 10 mm. SEM images were visualized with ImageJ software.

## 2.6. Mechanical Tests

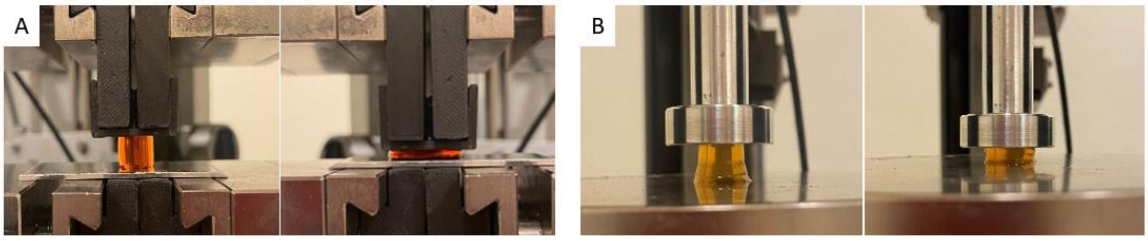


Figure 6: Mechanical Test of Before (A) and after swelling (B) of hydrogels

Uniaxial compression measurements were performed on both swollen and unswollen specimens of Alg-Tyr-Gel and Cmc-Tyr-Gel hydrogels using a universal testing machine (Zwick Roell) equipped with a 200 N load cell. The casted gel specimens were prepared in cylinder form with the dimensions of 9 mm in diameter and 10 mm in length for the compression tests as shown in Figure 10. The measurements were conducted at strain rates of 5 $mm.min^{-1}$ at 23 ± 2 $^{o}C$ up to 90% deformation. The linear region of the stress-strain curve between 4 and 6 % compression was used to calculate Young's modulus *E* of the specimens. In the strain-stress curves, nominal stress was plotted as a function of the deformation ratio.

## 2.7. FTIR analysis

The infrared spectra of Tyramine, Alg-Tyr, and Cmc-Tyr conjugate specimens were analyzed with Shimadzu Fourier-transform infrared spectroscopy (FTIR) spectrophotometer (Thermo-Nicolet iS10) equipped with an attenuated total reflectance (ATR) accessory at room temperature. Their FTIR spectra were examined at a resolution of 4 $cm^{-1}$ and in the wavenumber range of 600-4000 $cm^{-1}$.

## 2.8. Cell Culture and Differentiation

Cryopreserved passage 2 bone marrow-derived hMSCs were provided from ATCC. Cells were cultivated for two passages (P4) in the Mesenchymal Stem Cell Basal Medium supplemented with Mesenchymal Stem Cell Supplement Kit, 10% FBS, and 1% antibiotics. The cells were cultivated at 37 °C in a humid environment with 5% $CO_2$. The culture medium was refreshed every three days and the cells were passaged using trypsin-EDTA when they were 80–90% confluent.

Casted hydrogels were incubated for three weeks in different culture media: for osteogenic differentiation performed in the Osteocyte Differentiation Tool and for

chondrogenic differentiation medium composed of StemPro™ Chondrogenesis/osteogenesis Basal Medium with Chondrogenesis Differentiation Kit. Both differentiation mediums were supplemented additional supplements for 10% FBS and 1% antibiotics. Bioprinted hydrogels were cultured for three weeks in a mixed medium of %50 osteogenic and %50 chondrogenic differentiation media and the media were refreshed every 3 days.

### 2.9. Cell Proliferation and Morphology

The viability of cells was evaluated on days 1, 3, and 7 by staining with the Calcein acetoxymethyl ester (Calcein-AM) and propidium iodide (PI) to assess the cytotoxicity of the bioprinting processes. The structures were dyed for 30 minutes at 37 °C with 1 M calcein-AM (green fluorescence) and then for 5 minutes with 0.75 M propidium iodide (red fluorescence).

To display cellular morphology differences of the differentiated cells in the bioprinted structures were evaluated on 7, and 14. days by staining nuclei and f-actin. In brief, the bioprinted structures were fixated with 4% paraformaldehyde (PFA) for 60 minutes before being permeabilized with 0.1 percent Triton X-100 in PBS for 30 minutes. Finally, Alexa Fluor® 546 Phalloidin was used to stain the f-actin cytoskeleton for 60 minutes, and the nuclei of the cells were stained for 15 minutes in PBS with a (1:2000) ratio of 4′,6-diamidino-2-phenylindole (DAPI).

Three-dimensional cellular images taken by an inverted confocal microscope (Carl Zeiss LSM 710) were used to monitor cell viability and cellular morphology, with maximum excitation/emission wavelengths of 488/515 nm for viable cells, 561/625 nm for dead cells, 556/570 nm for f-actins, and 358/461 nm for nuclei staining.

### 2.10. Biochemical assays

ALP activity was measured on 1, 7, 14, and 21 days after cast Cmc-Tyr-Gel structures were lysate in M-PER ™ Mammalian Protein Extraction Reagent for 30 minutes at RT.

The lysis solutions were centrifuged at 14,000 rpm for 15 minutes, and the supernatants were taken and incubated in a 4-nitrophenyl phosphate (pNPP) substrate at 37C for 60 minutes after incubation absorbance was measured at 405 nm. The total protein amount of each sample was determined using the BCA Protein test kit. Briefly, BSA has a concentration range of 5-1000 g/mL and is used to create protein standards. The standard concentrations were measured at 595 nm, and the results of the BCA test were used to normalize the ALP activity per unit of protein content.

Quantifying sulfated glycosaminoglycan (sGAG) contents of cast Alg-Tyr-Gel hydrogels were examined on 1, 7, 14, and 21 days after with a 1,9-dimethyl methylene blue (DMMB) assay with chondroitin-4-sulfate as a standard. Firstly, samples lysed in 1 mL of 100 μg/ml protease K lysis buffer in 10 mM Tris/HCl adjusted pH 7.5 for 1.25 mg tissue. Briefly, 16 mg DMMB was dissolved in 1 liter DI water followed by the addition of 95 of ml 0.1M acetic acid, 1.6 g of 1 M NaCl, and 3.04 gr of Glycine. Samples were mixed with 1.25 ml DMMB dye for 30 minutes at RT and finally centrifuged at 10000 rpm for 15 minutes at 16°C. A 200 μl supernatant was withdrawn and measured at 595 nm. The standard curve was generated with chondroitin-4-sulfate serial dilution ranging from 0 - 800 μg/ml and after addition, DMMB dye for each concentration measured 525 nm.

## 2.11. Histology staining

The bioprinted and cast hydrogel structures were embedded in cryomedium for cryosectioning to collect histological sections after 21 days of incubation (Hruschka et al., 2013). For 4 hours, the specimens were fixed in a %4 paraformaldehyde solution. After cleaning with PBS samples, they were embedded with cryomedium and stored at -80 C overnight for frozen sectioning. Histological sections were created by slicing tissue with a cryotome using standard protocols ("CryoStor CS2, CS5, and CS10 Cryopreservation Media," 6222) and a thickness of 10-5 μm.

After sectioning Cmc-Tyr-Gel cast hydrogels revealed $Ca^{+}$ deposition staining with %1(w/v) Alizarin Red S (Sigma) adjusted pH.4.1 $NH_4OH$ in the dark and samples were

washed with %50 ethanol. Following sectioning, Alg-Tyr-Gel cast hydrogels were stained with 1% (w/v) Alcian Blue in 3% (v/v) acetic acid to demonstrate chondrocyte proteoglycan formation (Walker, 2009). After that, stained hydrogels were washed subsequently with a solution of 3% (v/v) acetic acid, 25% ethanol, and 50% ethanol.

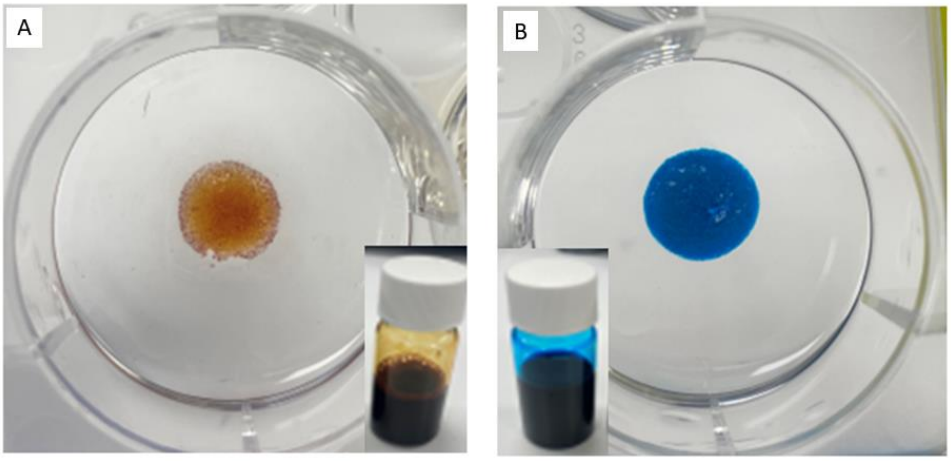


Figure 7: Biofabrication constructs after histology dyes A) Alizarin Red S dyed Cmc-Tyr-Gel B) Alcian blue dyed Alg-Tyr-Gel

Gradient hybrid multiline bioprinted structures were stained with both prepared Alizarin Red and Alcian Blue staining to confirm osteochondral interface. The section of the bioprinted structures were stained first with Alcian Blue solution then clear with the %50 ethanol solution to equalize ions charge and stained with Alizarin Red S solution. Finally, inverted light microscopy was used to capture images of all sectioning hydrogels from both casted and bioprinted samples.

## 2.12. Statistical analysis

The one-way analysis of variance (ANOVA) approach was used to determine whether any differences in the data for cell viability were statistically significant. P values of 0.05 or below ($P* < 0.05$, $P** < 0.01$) were deemed statistically significant.

## 2. Result and Discussion

### 3.1. Analysis of Alg-Tyr and Cmc-Tyr with FTIR technique

Alginate and Cmc were conjugated with tyramine molecules using carbodiimide chemistry to acquire bioactivity. The carboxylic groups of Alginate and Cmc were reacted with amine group of tyramine in the presence of EDC/ NHS coupling. Figure 12 shows the illustration of the conjugation reaction of alginate and Cmc with tyramine.

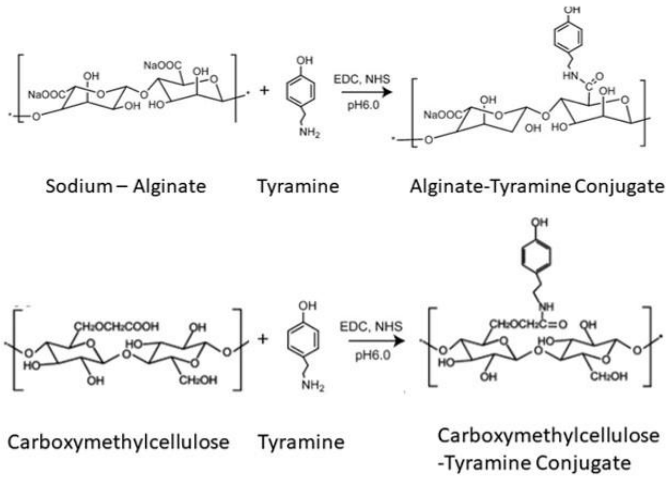


Figure 8: The scheme of the synthesis of Alg-Tyr and Cmc-Tyr.

The synthesis of Alg-Tyr and Cmc-Tyr conjugate specimens was qualitatively analyzed by the FTIR technique. To confirm tyramine conjugation of both alginate and Cmc, the infrared spectra of synthesized Alg-Tyr and Cmc-Tyr were compared with that of tyramine. Figure 13 A and B give The FTIR spectra of Alg-Tyr and Cmc-Tyr, respectively, together with that of tyramine.

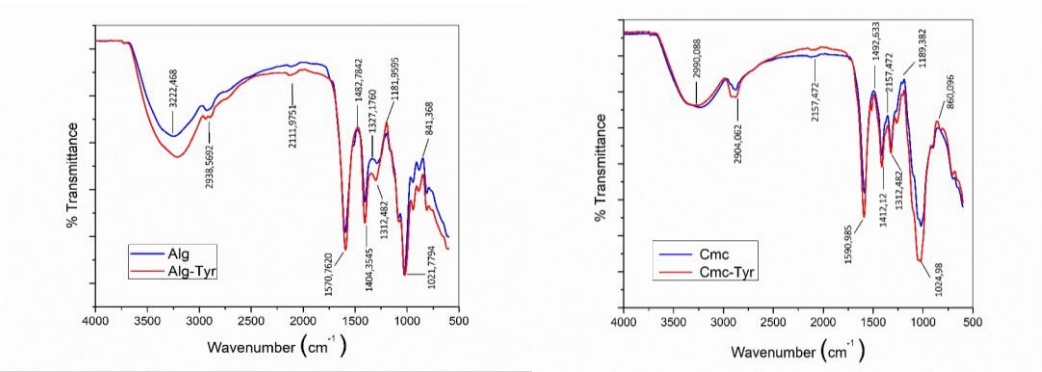


Figure 9: The FTIR spectra of (A) Alg-Tyr and (B) Cmc-Tyr precursors compared with that of tyramine.

FTIR spectrum of alginate display typical absorption bands of carboxyl, ether, and hydroxyl groups. The peaks at the 3224, 2938, and 1600-1400 $cm^{-1}$ were attributed to the vibration of OH bonds, the vibration of aliphatic CH bonds, and asymmetric and symmetric stretching vibrations of COO groups, respectively (Bajas et al., 2021). These bands also appeared in the FTIR spectrum of Alg-Tyr precursor. A distinctive peak confirming the conjugation of tyramine was at 1510 $cm^{-1}$, which was related to the stretching vibration of aromatic rings of tyramine (Prodanovic et al., 2015). This peak was only in the spectrum of Alg-Tyr, while it did not appear in that of Alg. FTIR spectrum of Cmc-Tyr precursor had similar typical absorption bands to those of Alg-Tyr, which corresponded to polysaccharides. The peak at 1510 $cm^{-1}$ was also seen in the spectrum of Cmc-Tyr, which is evidence of the conjugation of Cmc with tyramine. The gelation mechanism is shown in Figure 14.

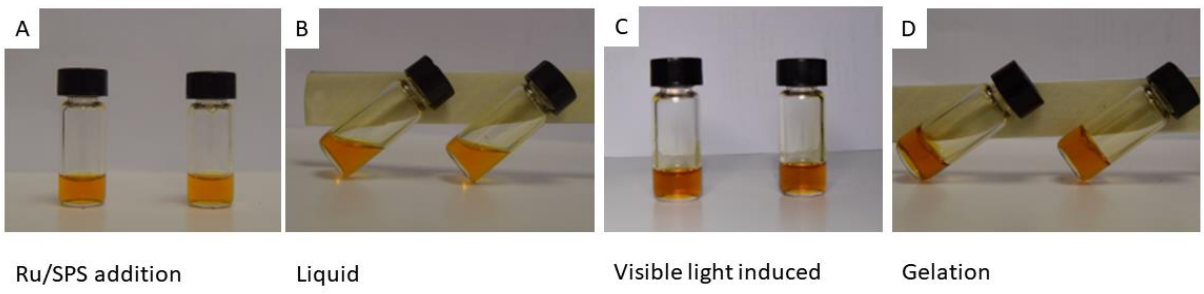


Figure 10: Gelation of Ru/SPS mechanism under visible light.

### 3.2. Morphological Analysis

The pore morphology of cell-laden printed structures is crucial for the formation of the cellular habitat that encourages cell growth/ proliferation and migration. Therefore, the porous structures of Alg-Tyr-Gel and Cmc-Tyr-Gel hydrogels were investigated with the SEM technique. The molded hydrogels were subjected to SEM measurements both in unswollen- and swollen-states because of the change in their pore sizes after swelling. Figure 15 gives the SEM images of all the samples of Alg-Tyr-Gel and Cmc-Tyr-Gel hydrogels in two different zoom scales.

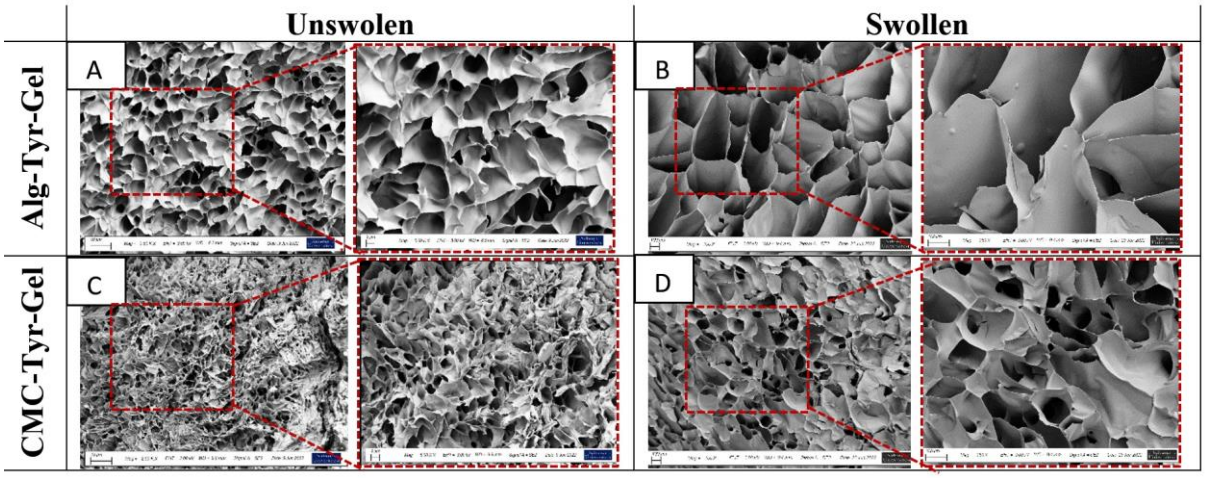


Figure 11: SEM images of (A,C) unswollen and (B,D) swollen Alg-Tyr-Gel and Cmc-Tyr-Gel hydrogels, respectively.

According to SEM results, pore diameters of Alg-Tyr-Gel and Cmc-Tyr-Gel hydrogels increased from $15 \pm x_i$ and $6 \pm y_i$ to $450 \pm x_{ii}$ and $300 \pm y_{ii}$, respectively, after swelling because of their enlargement by entering water into the pores. When compared to Cmc-Tyr-Gel hydrogels, the larger pore size of Alg-Tyr-Gel hydrogels before and after swelling tests may estimate further chondral differentiation specific collagen X content expression (Murphy & O'Brien, 2010). Besides, having a pore size of 200-700 m after swelling can be related to higher levels of chondrocyte differentiation (Lin et al., 2019). The heterogeneous distribution of Cmc-Tyr-Gel hydrogel pore structures between 100-500 m after swelling includes both the optimal pore size for bone growth (100-135 m) and the vascularization pore size (>300 m) required for long-term culturing (Murphy & O'Brien, 2010).The porous structures of all the samples have heterogeneous distribution. The SEM analysis of unswollen gel samples assisted to reveal the pore

difference between the hydrogels with Cmc and alginate, while those of swollen samples informed that the pores became suitable for cellular activities after swelling (Figure 16).

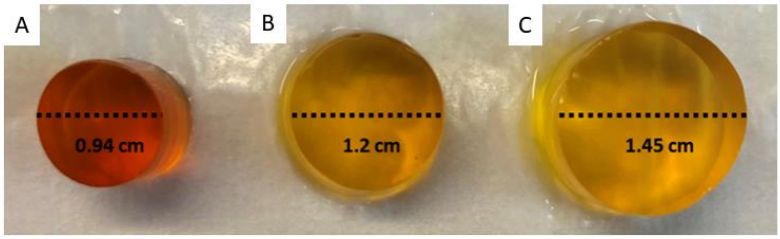


Figure 12: Before (A) and after swelling capacity differences between Cmc-Tyr-Gel (B) and Alg -Tyr-Gel (C).

### 3.3. Mechanical Properties

Mechanical properties of casted gel samples were investigated by uniaxial compression tests at 23 ± 2 °C. Figure 17 A and B present typical stress-strain curves of compression tests of the casted gels before and after swelling, respectively. Young's modulus, compressive strength, and fracture strain of the hydrogels are shown in Table 1. Young's moduli of both Alg-Tyr-Gel and Cmc-Tyr-Gel hydrogels decreased from 4.71 and 8.41 kPa to 1.40 and 1.46 kPa, respectively, after equilibrium swelling because entangled polymer chains became expanded with penetration of water inside the gel network. Their compressive strengths were also descended with the equilibrium swelling. On the other hand, Alg-Tyr-Gel hydrogel, which resisted up to 80% deformation in an unswollen state, was broken in 40% compressive strain after swelling, while Cmc-Tyr-Gel hydrogel in swollen state sustained its resistance up to around 80% compressive strain. Cmc-Tyr-Gel hydrogel exhibited mechanical stability by comparison to Alg-Tyr-Gel since the hydrogel including Cmc had a lower swelling degree than those with Alg.

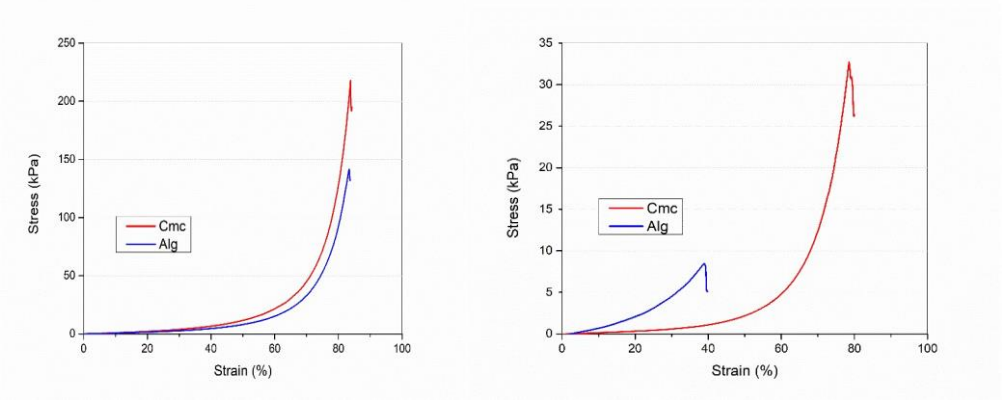


Figure 13: Stress-strain curves of Alg-Tyr-Gel and Cmc-Tyr-Gel hydrogels (A) before and (B) after equilibrium swelling. The curves of the hydrogels were indicated on the graphs.

Although stiffness does not alone determines cellular behavior, a matrix with about 1 kPa stiffness enforces both osteogenic and chondrogenic differentiation of human MSCs (Saghati et al., 2021). Moreover, mechanical stability is important for especially bone regeneration, because a mechanically non-stable matrix can cause endochondral bone formation (Zuscik et al., 2008).

### 3.4. Printability

Printability has also been related to extrudability, shape fidelity, and filament characterization which are essential terms used to describe bioink printability. In general, shape fidelity refers to a bioink's ability to retain its shape during and after deposition (Schwab et al., 2020). In this study, the dimensions of a single filament that can be printed in a single extrusion was limited by the length of the microcapillary glass tube is 7.5 cm used in the *in situ* crosslink printing system.

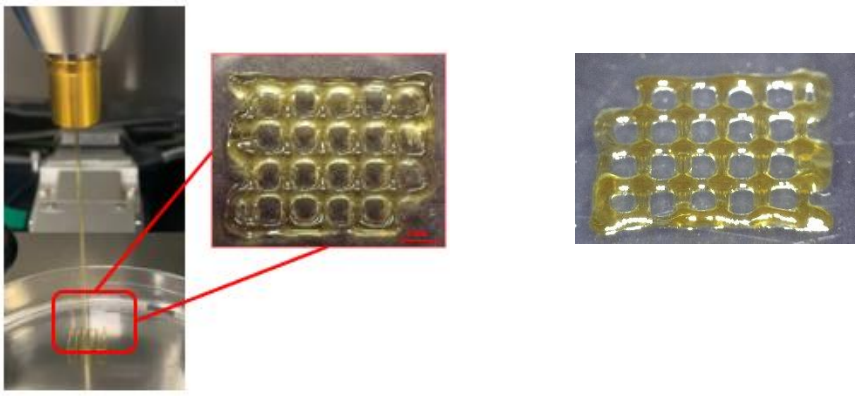

Figure 14: Printing grid design with microcapillary glass (A), and Grid design (B). The scale bar is 2 mm.

Grid design, one of the most common designs, was used for this evaluation in our printed structures. Figure 18 shows grid design, at least two layers are used, a 400 µm distance between the layers is left to allow for fusion, and extruded lines are rotated at 90° every other layer with 2 mm gaps. The success of grid printing, which previously achieved by Markstedt *et al* (Markstedt et al., 2017), based on the osteochondral anatomical shape predicted the printing precision in complex structures that could be designed in future studies.

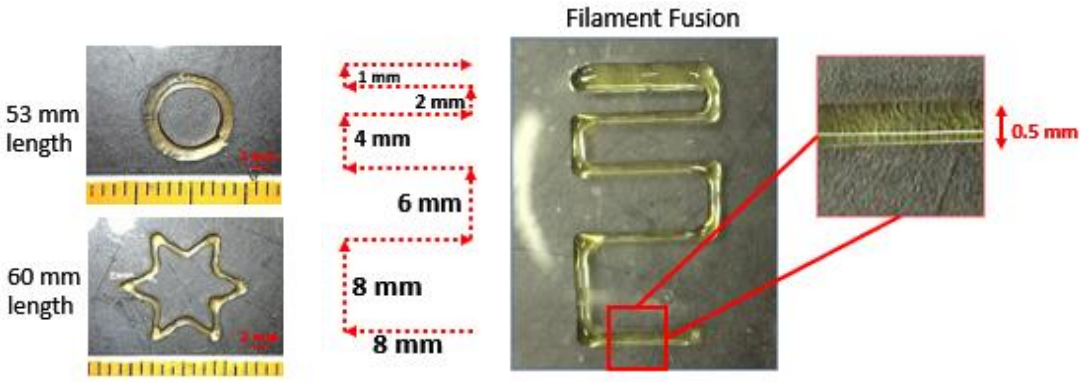


Figure 15: Singe filament shapes, Two offset circle (Ai), and Star (Aii) shapes. Flowing pattern with decreasing gap distance (Bi), Filament diameter (Bii). Scale bars are 2 mm.

A star shape was printed in addition to the grid structure to display fused segment length (fs) and filament thicknesses (ft) in printing, and a one-layered flowing pattern composed of parallel strands with decreasing gap distance was printed to investigate the filament fusion feature in Figure 19. The fusion between filaments was observed in the continuous printing that was inspired by the work (Cai et al., 2021) started with 8 mm

spacing, in spite of that no differences were found in filament segment length (fs) as the filament distance decreased.

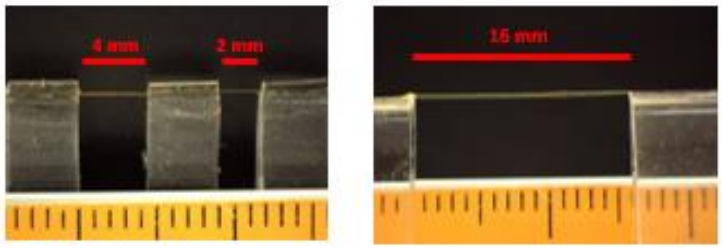


Figure 16: Filament collapse assay with 2, 4 mm (A), and 16 mm (B) gap size.

Specifically, biological hydrogels which are polysaccharides and/or proteins used in 3D bioprinting with *in situ* gelation have printability challenges about self-collapsing and deforming or rupturing on a single filament via their own weight (Lim et al., 2020). The filament collapse assay is creating hydrogel structures printed on the support having different gap lengths and related to angles formed between the unsupported filament and support parts and without noticeable deformation hydrogel structures printed on the gap of the support structure. A single printed hydrogel filament shows in Figure 20 a zero angle of collapse and no significant fractures or defects on the gap of support structure up to 16 mm.

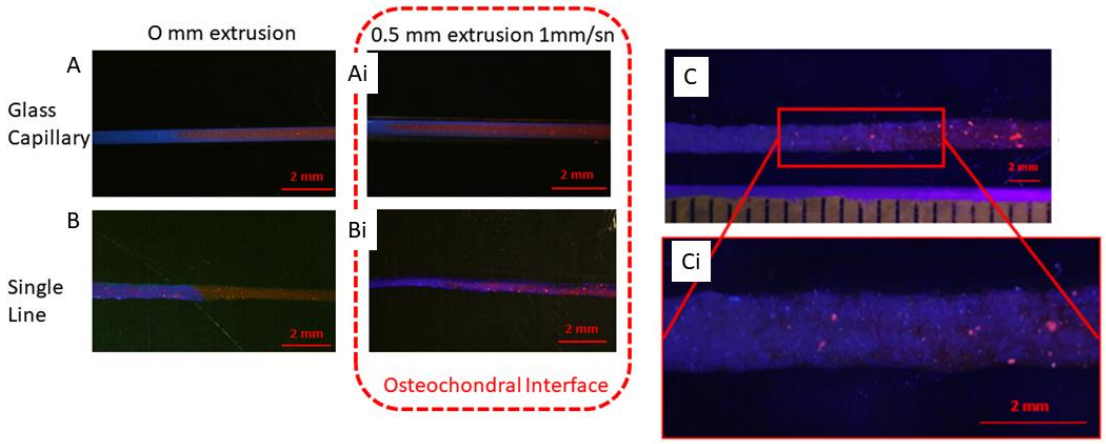


Figure 17: Microcapillary Glass images of different aspiration-extrusion printing method to create interfaces sharp distinct (A), and gradient (Ai). Single printed interfaces of a sharp distinct (B) and gradient (Bi). Serial multiline printed gradient interface structure for chosen osteochondral tissue (C) and zoom-in gradient mixture (Ci).

Aspiration - extrusion printing method applied before *in situ* gelation was used to create a gradient hybrid interface. Sharp distinct and gradient interface areas were created with the different aspirating methods of the Cmc-Tyr-Gel and Alg-Tyr-Gel inks materials which were marked with fluorescent dye prepared separately. Since the interface areas were formed in the microcapillary glass, both microcapillary glass and single filament printing were performed to analyze whether a deformation occurred during printing (Figure 21). In osteochondral tissue design, it was decided that the appropriate method to provide the natural environment of stem cells was the gradient interface, beside of this, multi-filament printings were carried out successfully (W. Wei & Dai, 2021). In this study, the hybrid structure is examined in microcapillary glass size, providing an improved perspective on the complex gradient of native osteochondral units.

## 3.5. Cell Experiments (proliferation, morphology, gene expression, biochemical assay, histology staining)

### *3.5.1.* Cell Viability

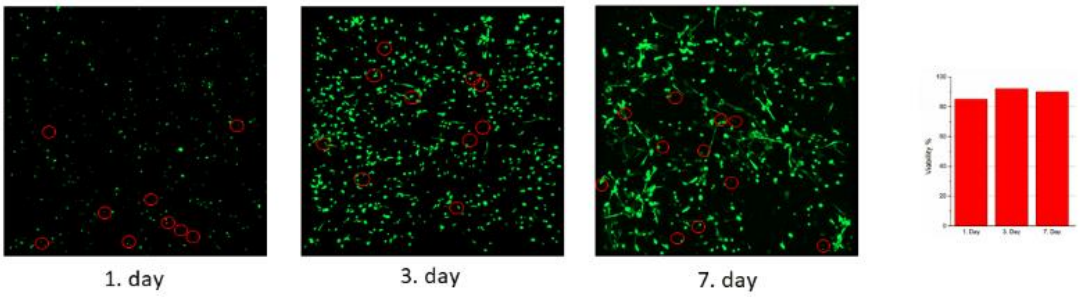


Figure 18: Cell viability of bioprinted structure 1 (A), 3 (B), and 7 (C) days. Live and dead cells are shown in green and red circles, respectively. Viability graph (D).

Cell-laden hydrogels were stained with Calcein-AM and PI to obtain cell viability after 1, 3, and 7 days of bioprinting. In living cells, acetoxymethyl ester hydrolysis by intracellular esterases converts calcein-AM dye to green fluorescence. Because live cells are impenetrable, PI can enter and stain DNA and RNA inside dead cells.

Hereby, green staining in 1, 3, and 7 days images indicates live cells, and red spots with red circles indicate dead cells. The cell viability was 85 ± 2.52% on day 1 and then increased to 95.76 ± 0.72% on day 3 (Figure 22). Any significant changes were not observed on day 7 with 93.81 ± 8.02% . Furthermore, the cell viability assay revealed no harmful effects and no cytotoxicity as a result of reactive by-products of the Ru/SPS catalyzed reaction during gelation. This study indicates that the Ru/SPS mediated crosslinking mechanism is appropriate for Biopolymers-Tyramine conjugates applications in a bioprinting approach.

### *3.5.2. Cell Morphology*

In the case of adherent cells' morphological and adhesion properties, such as osteoblasts and chondrocytes, determine their functional behavior and fate during stem cell differentiation. Particularly, culturing chondrocytes in a 3D environment rather than a 2D surface effects rounded cell morphology (Vyas et al., 2017).

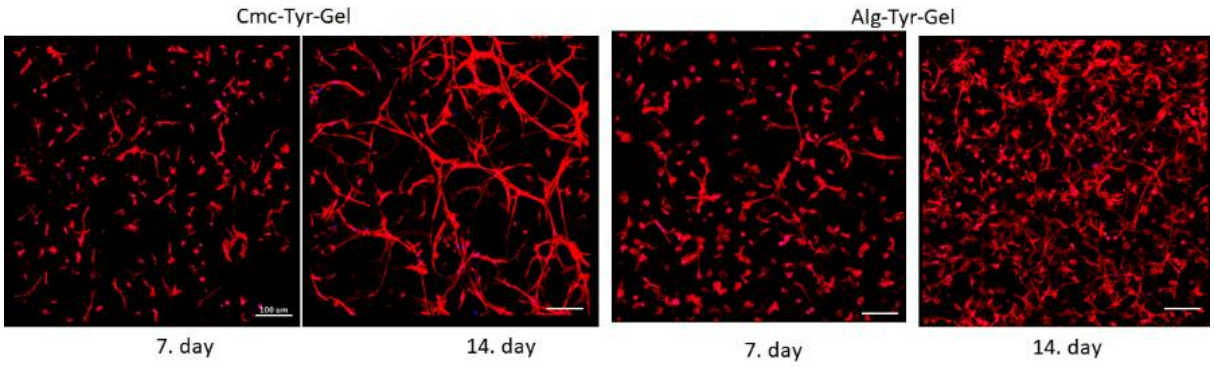


Figure 19: Cell morphology of osteogenic induced Cmc-Tyr-Gel hydrogel on 7 (A), 14 (Ai) days, and chondrogenic induced Alg-Tyr-Gel hydrogel on 7 (Bi), 14 (Bii) days.

Cmc-Tyr-Gel and Alg-Tyr-Gel bioprinted hydrogels were cultured separately to assess cellular morphology and phenotype differences were assessed using DAPI-Phalloidin staining. Cell nuclei were stained blue with DAPI staining, while cellular filamentous actins were stained red with Phalloidin staining at 7th and 14th-day cultures of specimens (Figure 23).

Initially, from the confocal pictures when comparing the 7th day of both bioprinted hydrogels, as seen in the images, the cells maintained their hMSC-like morphology and did not show significant differences in terms of phenotypic differences. In the following 14th-day culture, it was observed that the cells in the Cmc-Tyr-Gel hydrogel cultured with bone exchange medium had aligned fibrillary organization and were similar to the natural osteonal structure. In contrast, rounded morphology cells in Alg-Tyr-Gel hydrogel images cultured with cartilage medium clearly exhibit more of their native chondrogenic morphology. Therefore, MSCs cell-laden bioprinted hydrogels achieved differentiation cells into osteogenic and chondrogenic phenotypes when cultured in special different mediums by promoting various material properties such as stiffness and swelling.

### *3.5.3.* Biochemical Assay of Differentiation

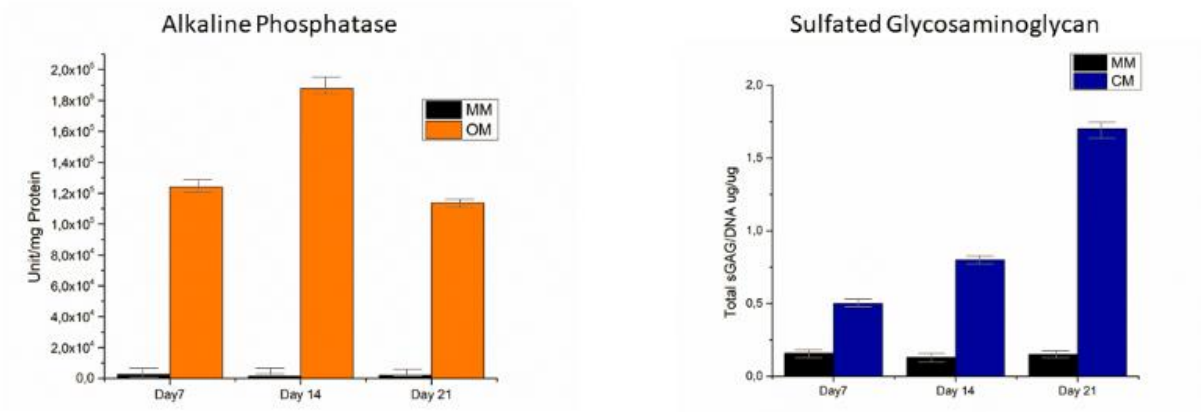


Cmc-Tyr-Gel Alg-Tyr-Gel

Figure 20: Alkaline phosphatase (ALP) enzymatic activity for osteogenic differentiation of Cmc-Tyr-Gel (A) and sulfated glycosaminoglycan (sGAG) assay for chondrogenic differentiation of Alg-Tyr-Gel (B) after 7, 14, and 21 days.

Calorimetric determination of alkaline phosphatase (ALP) enzyme, which is active in alkaline media, is a widely accepted marker of early osteogenic differentiation (de Melo Pereira et al., 2020). p-NPP, a colorless substrate, is phosphorylated by ALP to form the product p-nitrophenol (p-NP) whose yellow absorbance can be measured (Walker, 2009). In this study, ALP enzyme activity was measured in Cmc-Tyr-Gel cast hydrogels containing hMsc cells to show differentiation at 7, 14 and 21 days of osteogenic

stimulation of hMSc. Cmc-Tyr-Gel hydrogels cultured in Mesenchymal stem cell medium without differentiation medium were used as control group. Compared to the control group MM seen in Figure 24-A, ALP activation in osteogenic differentiated OM was significantly increased by 1.2 and 2.0 105 U/mg until day 7 and day 14, respectively. On the 21st day, while the ALP activation value in control MMs remained nearly constant, the concentration value in OMs decreased to 1.2 U/mg. Associating ALP enzyme activation with early osteoblasts, the decrease in the value measured on the 21st day can be considered as an indication that osteoblasts have passed into the late phase. As a result of ALP enzyme activation values, cellular response to Cmc-Tyr-Gel hydrogel has been shown to be suitable structures for bone tissue differentiation.

Glycosaminoglycans GAGs are long disaccharides that consist of negatively charged carboxylate/sulfate organizations that support chondrocytes and adhere to other matrix components. The 1,9-dimethyl methylene blue (DMMB) assay is commonly used to determine the quantity of sulfated glycosaminoglycan (sGAG) in MSCs during chondrogenic differentiation(C. Zheng & Levenston, 2015).

In this study, the amount of sGAG was determined on the 7th, 14th, and 21st days using a cast Alg-Tyr-Gel hydrogel chondrogenic differentiation medium. Chondrogenic differentiation was compared to a control group cultured only with a mesenchymal stem cell medium over the period. In differentiated CMs shown in the Figure 24-B , the rate of sGAG formation doubled on day 14 compared to day 7, while on day 21 it increased significantly to almost quadruple to 2 value. Despite this, sGAG levels in control MMs remained constant in all measurements until 21 days and were very poor in comparison to the differentiation medium. sGAG contents values show that the Alg-Tyr-Gel hydrogel provides a suitable environment for chondrogenic differentiation, beside demonstrates a certain potential increase depending on the time of culturing.

### *2.5.4 Histology Staining*

Specifically, the chondrogenic and osteogenic regions had different ECM content such as higher content of sGAGs and calcium nodules respectively, and investiagtion of their different components histological analysis is usually applied such as Alcian Blue or Alizarin Red S (Gadjanski & Vunjak-Novakovic, 2015; Joseph et al., 2017).

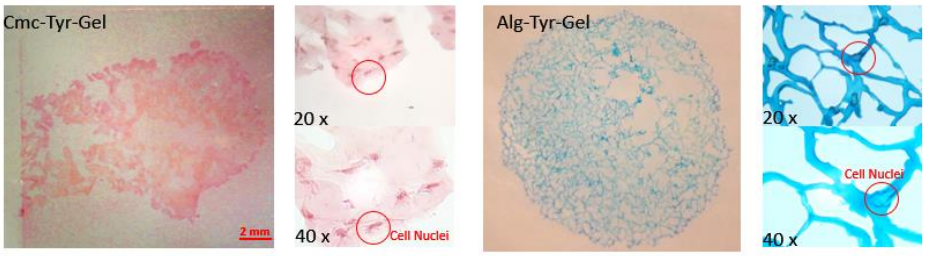


Figure 21:Alizarin Red S staining of osteogenic induced Cmc-Tyr-Gel (A), zoom in 20x (Ai), and 40x (Aii). Alcian Blue staining of chondrogenic induced Alg-Tyr-Gel (B), zoom in 20x (Bi), and 40x (Bii). Red circles are representative of cell nuclei.

Alizarin Red S, an anionic dye, turns red pigmented in the presence of calcium, allowing the observation of osteocytes in differentiated. After mono cultured osteogenic induction for 21 day, Cmc-Tyr-Gel cast hydrogels were stained with Alizarin Red S to analyze extracellular matrix (ECM) mineralization as shown in Figure 25. The results show that the ECM of the Cmc-Tyr-Gel hydrogel material composition exhibited red pigment for Alizarin Red S staining, suggesting that hMsc showed osteoblastic characteristics after 3 weeks of osteogenic incubation. The potential of chondrogenic cultured hMsc-laden hydrogel constructions are investigated using anionic Alcian Blue dye. After 21 days of chondrogenically incubation, cast Alg-Tyr-Gel hydrogels demonstrated high sulfated sGAG expression using Alcian Blue dye in Figure 25.

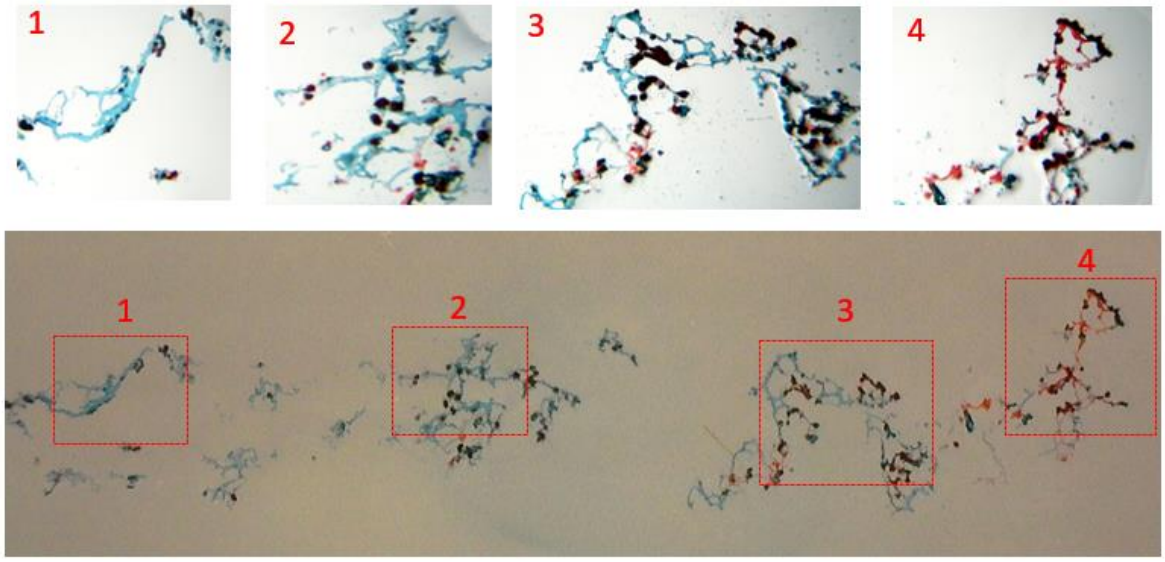


Figure 22: Co-cultured gradient hybrid bioprinted structure stained sectioning both Alizarin Red S and Alcian Blue.

Alizarin Red S and Alcian Blue dyes were applied to the same sectioning parts to further evaluate the capability of ECM accumulation differentiating hMSCs into various lineages in co-cultured bioprinted hydrogel constructs. Increasing gradient concentration of Alizarin Red S dye in bioprinted structures shows that the Cmc-Tyr-Gel portion supports osteogenic differentiation in two different material printing. However, the staining of the structure by the Alcian Blue dye proves the presence of sGAG expression in the Alg-Tyr-Gel side of bioprinted structure and supports differentiation chondrogenic when the co-culture is incubated. As the histology-stained images (Figure 26) of co-cultured bioprinted structures progressed from region 1 to region 4, the concentration of the red dye increased and the ratio of the blue dye decreased, proving that Cmc-Tyr-Gel and Alg-Tyr-Gel bioinks promoted the hMscs successfully differentiated into osteogenic and chondrogenic tissue in 21 days.

# 3. Conclusions and Future Works

Recent advances in tissue engineering have shown great promise for fabrication of soft and hard tissue structures such as cartilage and bone. Despite recent advancements in bioprinting process with cell-laden hydrogels, fabricating hybrid soft and hard tissue structures with a controlled interface has been a challenge.

In this study, a gradient hybrid structure was successfully created by utilizing a novel bioprinting with *in situ* crosslink technique, which mimics the physiochemical and mechanical characteristics of the osteochondral interface. Mesenchymal stem cells encapsulated in Cmc-Tyr-Gel and Agl-Tyr-Gel hydrogels were induced osteogenic and chondrogenic to demonstrate their suitability for the differentiation of structures into tow different tissues, namely bone and cartilage. Histological analyses showed that the hybrid bioprinted gradient structures co-cultured in a mixed differentiation medium differented into chondrogenic and osteogoenic cells with mechanical and chemical cues. Our findings lead to future research by revealing the high resolution of the print structure with two distinct regions, demonstrating the potential of this approach for osteochondral tissue interface application.

One of the limitations of using 3D bioprinting is the lack of more suitable materials for the development of studies on OC tissue regeneration. To overcome these limitations, conjugated hybrid hydrogels that supports bioactive chondrogenic and osteogenic differentiation have been developed and used in the developed biofabrication method. The success of the in-situ crosslink mechanism, which enables for the replication of gradient composition within OC tissue, is a key feature for fabrication of other types of hybrid tissue interfaces in the future.

# Chapter 2

## 4. Introduction

Recent improvements in bioprinting technology, which rely on the layer-by-layer deposition of cell-laden materials in desired geometries, have made essential contributions to regeneration medicine and tissue engineering for the mimicking of hybrid natural tissues and organs (Setayeshmehr et al., 2019) and especially repair of OC tissue (Gadjanski & Vunjak-Novakovic, 2015). As mentioned beofere, extrusion-based printing, in which the extrusion of bioinks via pneumatic or mechanical pressure, has been frequently used in tissue engineering (Ozbolat & Hospodiuk, 2016). 3D bioprinting complex structures with overhangs and internal features using soft hydrogels is a challange. Support baths are currently used to address this problem. In this embedded printing approach, an ink solution is deposited into a support bath, which enables a temporary frame to protect the deposited ink structure throughout the extrusion process. The approach allows for the gelation of liquid reaction mixture during and/or after the printing process, providing for the manufacturing of hydrogel-based complex 3D constructs with high fidelity. To print complex-shaped 3D structures, a variety of materials have been used as a support bath component, including Laponite, gellan, carbopol, and gelatin slurry (Moustafa & Abd- El- Hakim, 1977; S. Paul & Ranby, 1976; T. K. Paul et al., 1982). Gelatin methacrylate (GelMA), the photo-crosslinkable derivative of gelatin, is of special biomaterials among the natural hydrogel due to its biocompatibility, biodegradability, and cell-responsive properties. Because GelMA is a gelatin-based hydrogel, a new bioprinting approach that allows cell-friendly

and one-step gelation for crosslinking while retaining the same bioactive and mechanical properties is required.

The ability of bisulfite and metabisulfite to induce the polymerization of certain vinyl monomers in an aqueous system, such as methyl methacrylate, ethyl methacrylate, and methacrylic acid, has been documented in scientific studies. In a similar way to the bisulfite-persulfate redox system, radical formation is the basis of the initiation mechanism (Van Den Bulcke et al., 2000). According to Mukherje et al., the methacrylate groups of the monomer with bisulfite or metabisulfite ions generate sterically hindered radicals and these radicals are less reactive than others. Therefore, bisulfite or metabisulfite ions cause to initiate only the selective monomers including methacrylate groups (Z. Wang et al., 2018).

In this study, we presented a novel crosslinking without the need of any photoinitiator which could be harmful for cells. This work provides an encouraging option for photo-induced and/or cell-damaging crosslinking mechanism of GelMA hydrogels to assist in 3D bioprinting methods. During the printing process, cell laden GelMA ink performs in situ crosslinking with required amount of bisulfite ions for gelation in the aqueous phase of the support bath via free radical polymerization. Additionally, we bioprinted constructs that show high cell viability and strong mechanical strength with the help of using the optimal SBS amount in the support bath. A shmetaica presentation of the proposed bioprinting method is shown in Figure 27.

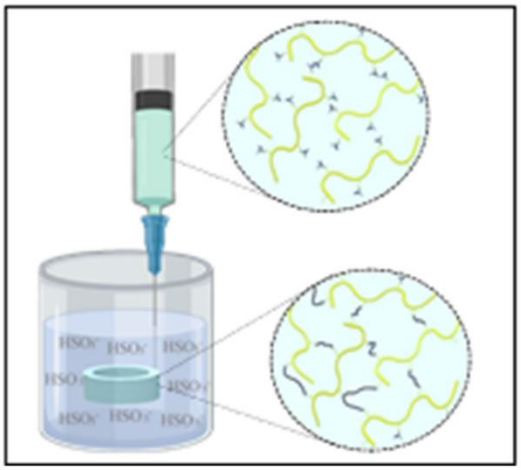

Figure 23: (A) Schematic of a bisulfite-initiated crosslinking technique for embedded 3D bioprinting of GelMA.

# 5. Materials and Method

## 6.1. Materials

Gelatin (type A, 300 bloom, porcine skin), sodium bisulfite (SBS), sodium bicarbonate (SBC), methacrylic anhydride (MA), nitric acid ($HNO_3$), hydrogen peroxide ($H_2O_2$), collagenase (IA, 125 CDU/mg), pluronic F127, tetrazolium salt WST-1 were purchased from Sigma-Aldrich. Sigma provided Dulbecco's Modified Eagle Medium - High Glucose (DMEM), fetal bovine serum (FBS), and N-(2-Hydroxyethyl) piperazine-N-(2-ethanesulfonic acid) (HEPES). Gibco provided penicillin-streptomycin, phosphate buffered saline (PBS), and Dulbecco's phosphate buffered saline (10X dPBS, without Ca and Mg). BYK Additives & Instruments supplied the Laponite RDS. Invitrogen supplied the calcein-AM and propidium iodide. AppliChem bought the Triton X-100. Life Technologies and Thermo Fisher bought Alexa Fluor® 546 Phalloidin and 4′,6-diamidino-2-phenylindole (DAPI). The American Type Culture Collection provided human dermal fibroblast (HDF) (ATCC).

## 6.2. Preparation of Hydrogel and Bioink

Molded gel samples were created with varying concentrations of SBS in order to characterize the GelMA hydrogel network. SBS ranged between 0.02 and 1 percent w/v, whereas GelMA concentration was set at 10 percent w/v mixed at 40ºc. Calculated dosage of SBS from bisulfite stock solutions was added to the GelMA solution. The 2 mm disposable syringes with the gel precursors were immediately filled. The hydrogels were taken out of the syringe after one day and used for measurements.

Human dermal fibroblast (HDF) were cultured in DMEM containing 10% FBS and 1% penicillin-streptomycin, and then incubated at 37 °C with 5% CO2 and 70–80% humidity to generate the cell line. 10 percent w/v GelMA solution was prepared by dissolving In HEPES buffer (0.3 M), and $1x10^6$ HDF cells per milliliter added to create bioink precursor solution.

## 6.3. Preparation of Support Bath

Accordance with the previously produced nano clay-hydrogel compound supporting media by Afghah et al., the support bath was created (Afghah et al., 2020). In this study, Pluronic F-127, Laponite RDS, and $CaCl_2$ were supplemented with SBS in replace of $CaCl_2$ to adapt the bath to the novel crosslinking method of GelMA. 10 percent (w/v) of pluronic F127, 3 percent (w/v) of laponite RDS, and 0.6 percent (w/v) of SBS compose up the support bath. In a brief, 10g of pluronic F127 were dissolved and mixed at 4 $^{o}$C for one day. Laponite RDS (3g) was dissolved in 50 ml of DW for an hour to create a laponite suspension. The laponite solution was combined with SBS (1g), and the mixture was stirred until homogenized. At room temperature, pluronic solvent was gradually added into the laponite-SBS solution. After eventually being incubated for one day at 37 $^{o}$C, the solution was ready for print.

## 6.4. Swelling and Degradation Tests

Hydrogel samples were immersed in PBS solution at 37 $^{o}$C for swelling tests on the hydrogels, and the solution was changed every other day. The samples were evaluated after equilibrium swelling in PBS, followed by lyophilized. Following the recording of the dry weight and swelling ratio, Qw was computed using the method below;

$$Q_w = \frac{w_s}{w_d} \qquad (1)$$

where $W_s$ and $W_d$ are equilibrium swollen and dried weights of the gel sample, respectively.

The hydrogels' enzymatic degradation tests were evaluated at using collagenase at an amount of 0.2 mg.mL$^{-1}$ in PBS. At periods of half an hour, their weight was recorded, and the amount of weight loss was calculated using the method below:

$$Weight\ Loss\ \% = \frac{w_o - w_t}{w_o} \times 100 \qquad (2)$$

where $W_o$ and $W_t$ are the weight of hydrogel samples at time 0 and at time t, respectively.

### 6.5. FTIR Measurements

To methodologically prove the methacrylation and crosslinking of GelMA, the infrared spectra of gelatin, the GelMA macromer, and the hydrogel specimens were analyzed by a Shimadzu FTIR spectrophotometer (IRAffinity-1S, USA). The FTIR spectra were obtained for each specimen in the ATR mode with a resolution of 4 $cm^{-1}$ and a wavenumber range of 800-4000 $cm^{-1}$.

### 6.6. Bioprinting of Cell-laden Bioink

A cylindrical structure with a 6 mm diameter and a 2 mm height was developed for the bioprinting. A 25 G nozzle was used to produce bioink at 28 $^{o}$C, 0.1 bar of printing pressure, and 300 mm/min of printing speed. The bioprinted constructions were obtained out of the support bath and cleaned with 1x dPBS following incubation for completed of crosslinking. The bioprinted structures were incubated in DMEM at 37 $^{o}$C.

### 6.7. Evaluation of Cell Viability

Using Calcein AM-PI staining, the viability of the cells in the GelMA bio-structures was assessed on days 1, 3, and 7. After cleaning with 1X dPBS, the samples were labeled with 0.75 M propidium iodide (red fluorescence) for 5 minutes in 1X dPBS at 37 °C and 1 M calcein-AM (green fluorescence) for 30 minutes. Carried out using the following inverted confocal microscope (Carl Zeiss LSM 710), the optimum excitation/emission wavelengths for live and dead cells, were measured to be 488/515 nm and 561/625 nm, respectively.

## 6.8. Cytocompatibility Test

After seeded cells were treated with the hydrogel extract, cell metabolism was assessed using the tetrazolium salt WST-1 colorimetric assay. The printed hydrogel samples were cultured in DMEM at a concentration of 0.2 gr/ml for 24 hours at 37 °C with stirring at 80 rpm in conformance with ISO 10993-5. In a 96-well plate, HDF cells were seeded at 104 cells per well and grown for 24 hours. After that, hydrogel extracts were applied to each cell seeded wells. Cultures in DMEM and cultures containing 5% DMSO, respectively, served as the negative and positive standards. Each well's medium was taken out and thoroughly cleaned with PBS after 24, 48, and 72 hours of incubation. Each well was stained in a medium containing 10% WST-1 for 3 hours. Consequently, the medium's absorbance at 450 nm was evaluated using an ELISA reader after tetrazolium salt was transformed into formazan in the live cells. Cell metabolic activity percent were determined using a normalized negative control.

## 6.9. Statistical Analysis

All of the cell viability data was given as mean standard deviation, and one-way ANOVA was used to analyze significant differences. P values below 0.05 were deemed statistically significant ($P^* < 0.05$, $P^{**} < 0.01$).

# 6. Result and Discussion

## 7.1. Assessment of Crosslinking Mechanism of GelMA with Bisulfite Ions

Understanding the crosslinking reaction of GelMA based on the bisulfite-initiated free radical mechanism demonstrated that the crosslinking reaction occurs in aqueous environments via a radical-initiated mechanism, as proposed by Mukherje et. al (Mukherjee et al., 1964). FTIR methods were used to study qualitatively the process that occurs on the methacrylate groups of GelMA (Figure 28).

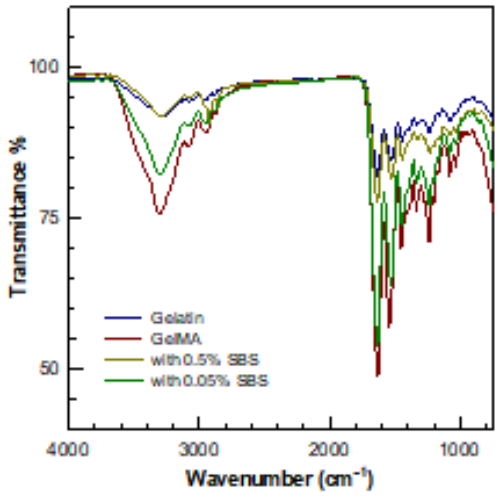


Figure 24: Gelatin, GelMA, and hydrogels FTIR spectra crosslinked with 0.5 and 0.05% SBS.

### *7.1.1. Swelling and Degradation Tests*

Hydrogel swelling and degradation properties are important elements that affect biological functions. The gel network's swelling behavior offers a good environment for

cells, while its breakdown feature supports the development and proliferation of tissue. The hydrogels were tested for swollen by submerging them in PBS at 37 $^{o}$C, and the weight-swelling rates of the hydrogels were displayed versus the proportion of SBS in Figure 29 A.

The swelling ratio between 12 and 15, remained unchanged significantly up to 0.1 percent SBS concentration. As illustrated in Figure 29 B, increasing the SBS concentration resulted in slower hydrogel degradation. Under the same degradation settings, hydrogels containing 0.02, 0.05, 0.1, 0.25, 0.5, and 1% SBS were totally destroyed after 2.5, 4, 4.5, 5, 6, and 6.5 hours, respectively.

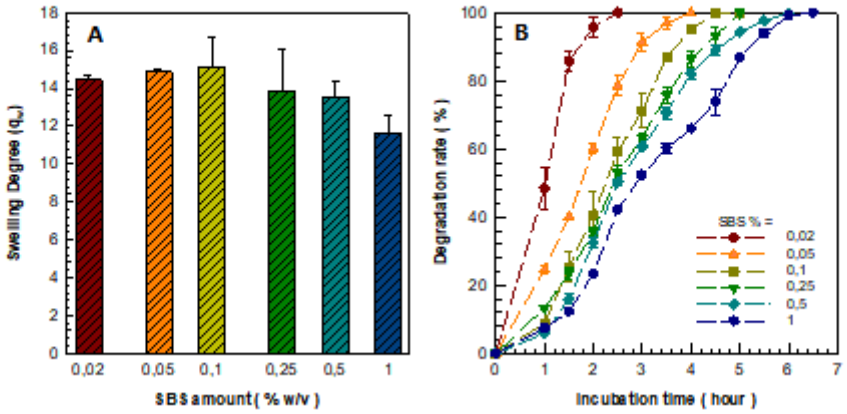


Figure 25: As a function of SBS concentration, (A) The rate of swelling of the hydrogels. (B) Enzymatic breakdown rate of hydrogels in PBS at 37 °C and 0.1 mg/ml collagenase solution.

### *7.1.2. 3D Bioprinting of Complex Constructs*

A custom made 3D bioprinter was used to biomanufacture complicated structures. Following CAD modeling and calculating path planning, extruded ink precursor was deposited into a support bath in the shape of the required models. To optimize printing parameters, a combination of varied feeding pressures, feed rate, and temperatures was employed to embed printing and create structures with excellent accuracy. By choosing the ideal parameters for each complicated design, the 3D structures at different scales were effectively printed without ink precursor leakage or damaging support bath self-recovery (Figure 30).

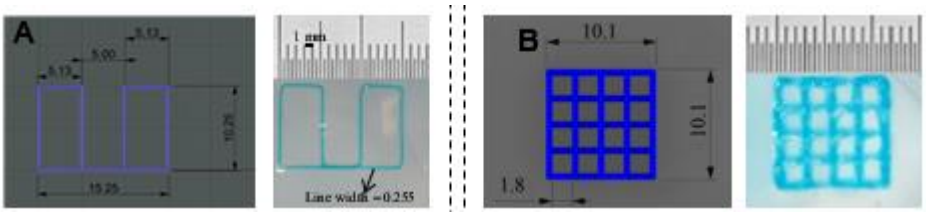


Figure 26: CAD models (on the left) and digital photos (on the right) of printed constructions with single layer (A) and grid (B) architectures.

By making the support bath compatible for our crosslinking reaction, SBS was used in place of $CaCl_2$ in the current support bath, leaving pluronic and laponite alone. Through extrusion-based printing, the GelMA and bisulfite ion crosslinking process successfully took place in the aqueous phase of the current bath. By comparing the path length and nozzle diameter, form fidelity—also known as pattern preservation of the bioink during extrusion—was examined using a single filament (Figure 30). The length of the fused sections served as further validation for filament fusion. According on the nozzle diameter, the extrusion pressure was adjusted, and lower values were chosen to avoid doing any serious damage to the cellular viability while bioprinting. The characterization of the feed rate prevented the development of discontinuous and non-uniform fibers. All printability studies were done on single fiber, grid, and hollow cylinder constructions.

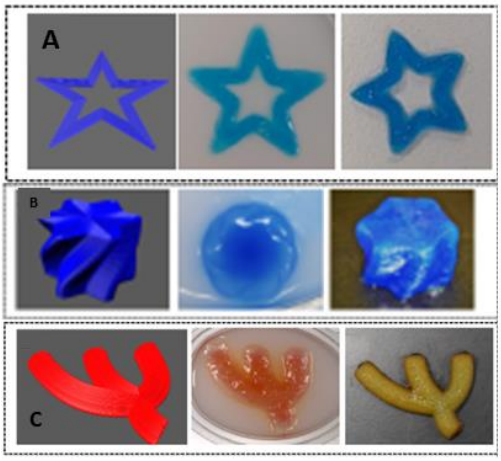


Figure 27: Images of complex-shaped objects besides stars (A), regular stars (B), and twisted stars (C), as well as a three-branched vessel (D).

Figure 31 shows star, twist, and branching vascular-like structures in CAD models, top and side perspectives, and both before and after being removed from the support bath.

After the printing, complex-shaped structures were removed from the bath by distilled water. For bioprinting of bioink with cells, controlling SBS content in the support bath is crucial since unreacted bisulfite ions can be harmful to cells if used excessively. In this study, the optimum solution SBS concentration was determined for the fabrication of the printed structures with high viable cells as well as excellent mechanical strength.

### *7.1.3. Cell Viability*

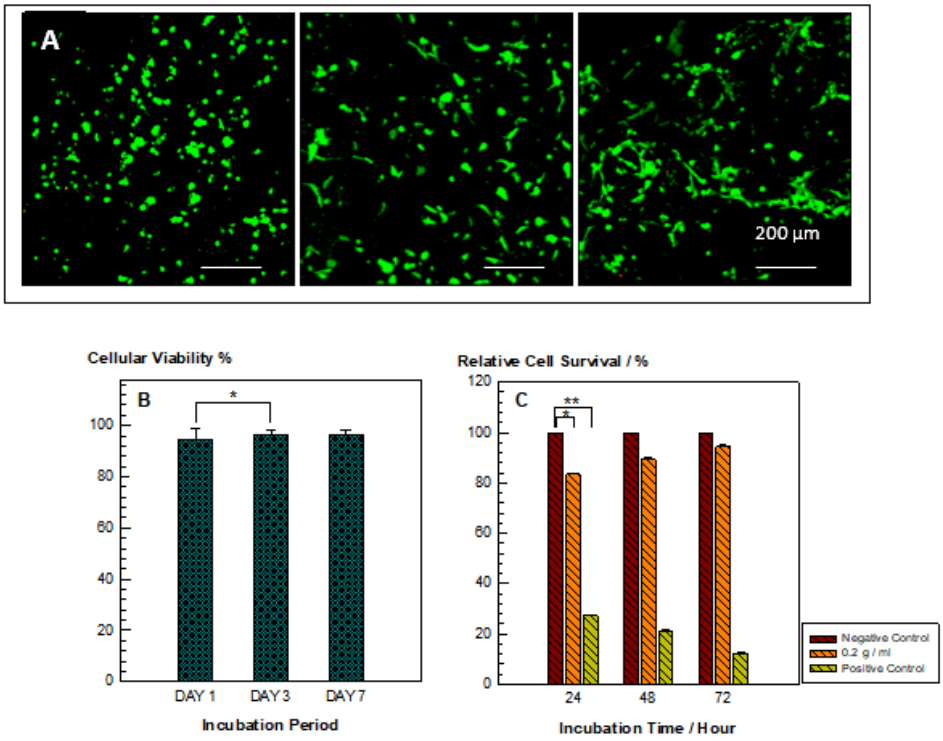


Figure 28: (A) Confocal microscopy pictures of GelMA bio-structure cells on days 1, 3, and 7, with a scale bar of 0.2 mm. (B) Quantitative cellular viability analysis on days 1, 3, and 7. (C) WST-1 assay.

Following the biofabrication process, the cell toxicicity of the crosslinking mechanism in the support bath was evaluated using a live/dead test. On days 1, 3, and 7 cellular viability was shown in Figure 32. Viability was 94.6 percent on day 1 and increased to 96 percent on day 3. Day 7 had a change of 96.5 percent, which was slightly different. The results in Figure 32 (B) showed how the crosslinking technique and the support bath, when combined with GelMA's exceptional encapsulation qualities, enhanced cell viability.

The mitochondrial dehydrogenase enzyme's activity detected by the WST-1 test as a decrease in the concentration of the soluble purple formazan dye. To demonstrate that no chemicals have leaked from the bioprinted structures after printing and washing, MTT data, particularly those from the first three days, are necessary. As a result, the experiment's measurement of a greater dye concentration shows in three days more cell growths on the well surface. When compared to control groups seeded three days later, there was no appreciable difference in the effects of exposure to extracts of the bioprinted GelMA samples on cell viability, with a survival rate of 93.4 percent. While viability decreases by 83.4 percent on the first day, it rapidly increases to 89.3 percent following 48 hours of incubation.

## 7. Conclusion & Future Works

The UV-induced gelation mechanism, which is frequently exploited in the GelMA crosslink method, could be harmful for cells. We developed a novel gelling method to prevent this harmful effect during bioprinting. Due to the interaction of methacrylate groups on the GelMA strand with bisulfite ions via free radical polymerization, this technique paired with embedded bioprinting technique enabled biofabrication of cell-laden and dimensionally complicated constructions.

During the embedded bioprinting process, GelMA is crosslinked *in-situ* with bisulfite ions in the support bath solution. The suggested printing method allows for one-step gelation of GelMA hydrogel lack of any photo-stimulus, allowing simple and cytocompatible biofabrication of complex structures. Dimensionally complicated shapes can also be effectively manufactured due to the quick crosslinking reaction that occurs during the ink's passage through the bath. Furthermore, the simple adaption of the current gelation approach to the embedded bioprinting technology will greatly aid in the production of complicated GelMA constructions further osteochondral tissue engineering.

Combining embedded bioprinting with bisulfite-initiated gelation resulted in greater cell viability for GelMA biofabrication, as well as advanced printability of cell-laden

structures and thus structural complexity. This advancement not only removes light on future hybrid bioprint research, but it also contributes to the printing of continuous gradient hybrid complex structures. Although this structure has an impact on the new crosslinking approach for GelMA in embedded bioprinting, the same crosslink mechanism can be used for other biopolymers for the development of the osteochondral complex interface.

## 8. References


Afghah, F., Iyison, N. B., Nadernezhad, A., Midi, A., Sen, O., Saner Okan, B., Culha, M., & Koc, B. (2022). 3D Fiber Reinforced Hydrogel Scaffolds by Melt Electrowriting and Gel Casting as a Hybrid Design for Wound Healing. *Advanced Healthcare Materials*, *11*(11), 1–16. https://doi.org/10.1002/adhm.202102068

Ahearne, M., & Kelly, D. J. (2013). A comparison of fibrin, agarose and gellan gum hydrogels as carriers of stem cells and growth factor delivery microspheres for cartilage regeneration. *Biomedical Materials (Bristol)*, *8*(3). https://doi.org/10.1088/1748-6041/8/3/035004

Ahmadian, M., Khoshfetrat, A. B., Khatami, N., Morshedloo, F., Rahbarghazi, R., Hassani, A., & Kiani, S. (2021). Influence of gelatin and collagen incorporation on peroxidase-mediated injectable pectin-based hydrogel and bioactivity of fibroblasts. *Journal of Biomaterials Applications*, *36*(1), 179–190. https://doi.org/10.1177/0885328220977601

Al-Abboodi, A., Tjeung, R., Doran, P. M., Yeo, L. Y., Friend, J., & Yik Chan, P. P. (2014). In Situ Generation of Tunable Porosity Gradients in Hydrogel-Based Scaffolds for Microfluidic Cell Culture. *Advanced Healthcare Materials*, *3*(10), 1655–1670. https://doi.org/10.1002/adhm.201400072

Aljohani, W., Ullah, M. W., Zhang, X., & Yang, G. (2018). Bioprinting and its applications in tissue engineering and regenerative medicine. *International Journal of Biological Macromolecules*, *107*(PartA), 261–275. https://doi.org/10.1016/j.ijbiomac.2017.08.171

Ashammakhi, N., Ahadian, S., Zengjie, F., Suthiwanich, K., Lorestani, F., Orive, G., Ostrovidov, S., & Khademhosseini, A. (2018). Advances and Future Perspectives in 4D Bioprinting. *Biotechnology Journal*, *13*(12), 1–12. https://doi.org/10.1002/biot.201800148

Athanasiou, K. A., Eswaramoorthy, R., Hadidi, P., & Hu, J. C. (2013). Self-organization and the self-assembling process in Tissue engineering. *Annual Review of Biomedical Engineering*, *15*, 115–136. https://doi.org/10.1146/annurev-bioeng-071812-152423

Axpe, E., & Oyen, M. L. (2016). Applications of alginate-based bioinks in 3D bioprinting. *International Journal of Molecular Sciences*, *17*(12). https://doi.org/10.3390/ijms17121976

Bajas, D., Vlase, G., Grad, O. A., Vlase, T., & Avram, C. (2021). Formulation and Characterization of Alginate-Based Membranes for the Potential Transdermal Delivery of Methotrexate. *Polymers*, *13*(161).

Bensaïd, W., Triffitt, J. T., Blanchat, C., Oudina, K., Sedel, L., & Petite, H. (2003). A biodegradable fibrin scaffold for mesenchymal stem cell transplantation. *Biomaterials*, *24*(14), 2497–2502. https://doi.org/10.1016/S0142-9612(02)00618-X

Bialik-Wąs, K., Królicka, E., & Malina, D. (2021). Impact of the type of crosslinking agents on the properties of modified sodium alginate/poly(Vinyl alcohol) hydrogels. *Molecules*, *26*(8), 7–10. https://doi.org/10.3390/molecules26082381

Bicho, D., Pina, S., Oliveira, J. M., & Reis, R. L. (2018). In vitro mimetic models for the bone-cartilage interface regeneration. *Advances in Experimental Medicine and Biology*, *1059*, 373–394. https://doi.org/10.1007/978-3-319-76735-2_17

Bishop, E. S., Mostafa, S., Pakvasa, M., Luu, H. H., Lee, M. J., Wolf, J. M., Ameer, G. A., He,

T. C., & Reid, R. R. (2017). 3-D bioprinting technologies in tissue engineering and regenerative medicine: Current and future trends. *Genes and Diseases*, *4*(4), 185–195. https://doi.org/10.1016/j.gendis.2017.10.002

Boys, A. J., McCorry, M. C., Rodeo, S., Bonassar, L. J., & Estroff, L. A. (2017). Next generation tissue engineering of orthopedic soft tissue-to-bone interfaces. *MRS Communications*, *7*(3), 289–308. https://doi.org/10.1557/mrc.2017.91

Cai, F. F., Heid, S., & Boccaccini, A. R. (2021). Potential of Laponite® incorporated oxidized alginate–gelatin (ADA-GEL) composite hydrogels for extrusion-based 3D printing. *Journal of Biomedical Materials Research - Part B Applied Biomaterials*, *109*(8), 1090–1104. https://doi.org/10.1002/jbm.b.34771

Castro, N. J., O'Brien, J., & Zhang, L. G. (2015). Integrating biologically inspired nanomaterials and table-top stereolithography for 3D printed biomimetic osteochondral scaffolds. *Nanoscale*, *7*(33), 14010–14022. https://doi.org/10.1039/c5nr03425f

Chang, C., Duan, B., Cai, J., & Zhang, L. (2010). Superabsorbent hydrogels based on cellulose for smart swelling and controllable delivery. *European Polymer Journal*, *46*(1), 92–100. https://doi.org/10.1016/j.eurpolymj.2009.04.033

Chen, J., Chen, H., Li, P., Diao, H., Zhu, S., Dong, L., Wang, R., Guo, T., Zhao, J., & Zhang, J. (2011). Simultaneous regeneration of articular cartilage and subchondral bone in vivo using MSCs induced by a spatially controlled gene delivery system in bilayered integrated scaffolds. *Biomaterials*, *32*(21), 4793–4805. https://doi.org/10.1016/j.biomaterials.2011.03.041

Chun, Y. Y., Wang, J. K., Tan, N. S., Chan, P. P. Y., Tan, T. T. Y., & Choong, C. (2016). A Periosteum-Inspired 3D Hydrogel-Bioceramic Composite for Enhanced Bone Regeneration. *Macromolecular Bioscience*, *16*(2), 276–287. https://doi.org/10.1002/mabi.201500258

Critchley, S., Sheehy, E. J., Cunniffe, G., Diaz-Payno, P., Carroll, S. F., Jeon, O., Alsberg, E., Brama, P. A. J., & Kelly, D. J. (2020). 3D printing of fibre-reinforced cartilaginous templates for the regeneration of osteochondral defects. *Acta Biomaterialia*, *113*, 130–143. https://doi.org/10.1016/j.actbio.2020.05.040

CryoStor CS2, CS5, and CS10 Cryopreservation Media. (6222). In *Sigma Aldrich*.

Cui, X., Breitenkamp, K., Finn, M. G., Lotz, M., & D'Lima, D. D. (2012). Direct human cartilage repair using three-dimensional bioprinting technology. *Tissue Engineering - Part A*, *18*(11–12), 1304–1312. https://doi.org/10.1089/ten.tea.2011.0543

Daly, A. C., Freeman, F. E., Gonzalez-Fernandez, T., Critchley, S. E., Nulty, J., & Kelly, D. J. (2017). 3D Bioprinting for Cartilage and Osteochondral Tissue Engineering. *Advanced Healthcare Materials*, *6*(22), 1–20. https://doi.org/10.1002/adhm.201700298

Daskalakis, E., Liu, F., Acar, A. A., Dinea, E.-E., Cooper, G., Weightman, A., Koç, B., Blunn, G., & Jorge Bártolo, P. (2020). 3D-Printed Composite Bone Bricks For Large Bone Tissue Applications. *MATEC Web of Conferences*, *318*, 01009. https://doi.org/10.1051/matecconf/202031801009

de Melo Pereira, D., Eischen-Loges, M., Birgani, Z. T., & Habibovic, P. (2020). Proliferation and Osteogenic Differentiation of hMSCs on Biomineralized Collagen. *Frontiers in Bioengineering and Biotechnology*, *8*(October), 1–16. https://doi.org/10.3389/fbioe.2020.554565

Dhawan, A., Kennedy, P. M., Rizk, E. B., & Ozbolat, I. T. (2019). Three-dimensional bioprinting for bone and cartilage restoration in orthopaedic surgery. *Journal of the American Academy of Orthopaedic Surgeons*, *27*(5), E215–E226.

https://doi.org/10.5435/JAAOS-D-17-00632

Farokhi, M., Shariatzadeh, F. J., & Solouk, A. (2020). Alginate Based Scaffolds for Cartilage Tissue Engineering : A Review Alginate Based Scaffolds for Cartilage Tissue Engineering : A Review. *International Journal of Polymeric Materials and Polymeric Biomaterials*, *69*(4), 230–247. https://doi.org/10.1080/00914037.2018.1562924

Fedorovich, N. E., Schuurman, W., Wijnberg, H. M., Prins, H. J., Van Weeren, P. R., Malda, J., Alblas, J., & Dhert, W. J. A. (2012). Biofabrication of osteochondral tissue equivalents by printing topologically defined, cell-laden hydrogel scaffolds. *Tissue Engineering - Part C: Methods*, *18*(1), 33–44. https://doi.org/10.1089/ten.tec.2011.0060

Findlay, D. M., & Kuliwaba, J. S. (2016). Bone-cartilage crosstalk: A conversation for understanding osteoarthritis. *Bone Research*, *4*(July). https://doi.org/10.1038/boneres.2016.28

Gadjanski, I., & Vunjak-Novakovic, G. (2015). Challenges in engineering osteochondral tissue grafts with hierarchical structures. *Expert Opinion on Biological Therapy*, *15*(11), 1583–1599. https://doi.org/10.1517/14712598.2015.1070825

Galarraga, J. H., Locke, R. C., Witherel, C. E., Stoeckl, B. D., Castilho, M., Mauck, R. L., Malda, J., Levato, R., & Burdick, J. A. (2022). Fabrication of MSC-laden composites of hyaluronic acid hydrogels reinforced with MEW scaffolds for cartilage repair. *Biofabrication*, *14*(1). https://doi.org/10.1088/1758-5090/ac3acb

Ganesh, N., Nair, S., & Nair, L. S. (2015). Bone-cartilage interface. In *Regenerative Engineering of Musculoskeletal Tissues and Interfaces*. Elsevier Ltd. https://doi.org/10.1016/B978-1-78242-301-0.00013-6

Gao, T., Gillispie, G. J., Copus, J. S., PR, A. K., Seol, Y.-J., Atala, A., Yoo, J. J., & Lee, S. J. (2018). Optimization of gelatin–alginate composite bioink printability using rheological parameters: a systematic approach. *Biofabrication*, *10*(3), 034106. https://doi.org/10.1088/1758-5090/aacdc7

GhavamiNejad, A., Ashammakhi, N., Wu, X. Y., & Khademhosseini, A. (2020). Crosslinking Strategies for 3D Bioprinting of Polymeric Hydrogels. *Small*, *16*(35), 1–30. https://doi.org/10.1002/smll.202002931

Gillispie, G., Prim, P., Copus, J., Fisher, J., Mikos, A. G., Yoo, J. J., Atala, A., & Lee, S. J. (2020). Assessment methodologies for extrusion-based bioink printability. *Biofabrication*, *12*(2). https://doi.org/10.1088/1758-5090/ab6f0d

Giuseppe, M. Di, Law, N., Webb, B., A. Macrae, R., Liew, L. J., Sercombe, T. B., Dilley, R. J., & Doyle, B. J. (2018). Mechanical behaviour of alginate-gelatin hydrogels for 3D bioprinting. *Journal of the Mechanical Behavior of Biomedical Materials*, *79*(September 2017), 150–157. https://doi.org/10.1016/j.jmbbm.2017.12.018

Goldring, M. B., & Cartilage, S. (2007). Bone and Osteoarthritis. In *Bone and Osteoarthritis* (Issue January). https://doi.org/10.1007/978-1-84628-701-5

Goldring, S. R., & Goldring, M. B. (2016). Changes in the osteochondral unit during osteoarthritis: Structure, function and cartilage bone crosstalk. *Nature Reviews Rheumatology*, *12*(11), 632–644. https://doi.org/10.1038/nrrheum.2016.148

Gonzalez-Fernandez, T., Tenorio, A. J., Campbell, K. T., Silva, E. A., & Leach, J. K. (2020). Evaluation of Alginate-Based Bioinks for 3D Bioprinting, Mesenchymal Stromal Cell Osteogenesis, and Application for Patient-Specific Bone Grafts. *BioRxiv*, 2020.08.09.242131. https://www.biorxiv.org/content/10.1101/2020.08.09.242131v1%0Ahttps://www.biorxiv.org/content/10.1101/2020.08.09.242131v1.abstract

Gopal, K., & Selvakumar, R. (2022). International Journal of Biological Macromolecules Tricomposite gelatin-carboxymethylcellulose-alginate bioink for direct and indirect 3D printing of human knee meniscal scaffold. *International Journal of Biological Macromolecules*, *195*(December 2021), 179–189. https://doi.org/10.1016/j.ijbiomac.2021.11.184

Guvendiren, M., Molde, J., Soares, R. M. D., & Kohn, J. (2016). Designing Biomaterials for 3D Printing. *ACS Biomaterials Science and Engineering*, *2*(10), 1679–1693. https://doi.org/10.1021/acsbiomaterials.6b00121

Habib, A., Sathish, V., Mallik, S., & Khoda, B. (2018). *3D Printability of Alginate-Carboxymethyl Cellulose Hydrogel*. https://doi.org/10.3390/ma11030454

Haldar, S., Lahiri, D., & Roy, P. (2019). 3D print technology for cell culturing. In *3D Printing Technology in Nanomedicine*. Elsevier. https://doi.org/10.1016/B978-0-12-815890-6.00005-0

Hammer, L., Van Zee, N. J., & Nicolaÿ, R. (2021). Dually crosslinked polymer networks incorporating dynamic covalent bonds. *Polymers*, *13*(3), 1–34. https://doi.org/10.3390/polym13030396

He, Y., Derakhshanfar, S., Zhong, W., Li, B., Lu, F., Xing, M., & Li, X. (2020). Characterization and Application of Carboxymethyl Chitosan-Based Bioink in Cartilage Tissue Engineering. *Journal of Nanomaterials*, *2020*. https://doi.org/10.1155/2020/2057097

Hoemann, C., Lafantaisie-Favreau, C.-H., Lascau-Coman, V., Chen, G., & Guzmán-Morales, J. (2012). The Cartilage-Bone Interface. *Journal of Knee Surgery*, *25*(02), 085–098. https://doi.org/10.1055/s-0032-1319782

Homenick, C. M., De Silveira, G., Sheardown, H., & Adronov, A. (2011). Pluronics as crosslinking agents for collagen: Novel amphiphilic hydrogels. *Polymer International*, *60*(3), 458–465. https://doi.org/10.1002/pi.2969

Hong, S., Kim, J. S., Jung, B., Won, C., & Hwang, C. (2019). Coaxial bioprinting of cell-laden vascular constructs using a gelatin-tyramine bioink. *Biomaterials Science*, *7*(11), 4578–4587. https://doi.org/10.1039/c8bm00618k

Hou, J., Li, C., Guan, Y., Zhang, Y., & Zhu, X. X. (2015). Enzymatically crosslinked alginate hydrogels with improved adhesion properties. *Polymer Chemistry*, *6*(12), 2204–2213. https://doi.org/10.1039/c4py01757a

Hruschka, V., Meinl, A., Saeed, A., Cheikh Al Ghanami, R., Redl, H., Shakesheff, K., & Wolbank, S. (2013). Gelatin embedding for the preparation of thermoreversible or delicate scaffolds for histological analysis. *Biomedical Materials (Bristol)*, *8*(4). https://doi.org/10.1088/1748-6041/8/4/041001

Huang, Y., Zhang, X. F., Gao, G., Yonezawa, T., & Cui, X. (2017). 3D bioprinting and the current applications in tissue engineering. *Biotechnology Journal*, *12*(8). https://doi.org/10.1002/biot.201600734

Jang, C. H., Lee, J. U., & Kim, G. H. (2019). Synergistic effect of alginate/BMP-2/Umbilical cord serum-coated on 3D-printed PCL biocomposite for mastoid obliteration model. *Journal of Industrial and Engineering Chemistry*, *72*(April), 432–441. https://doi.org/10.1016/j.jiec.2018.12.046

Jiang, J., Tang, A., Ateshian, G. A., Edward Guo, X., Hung, C. T., & Lu, H. H. (2010). Bioactive stratified polymer ceramic-hydrogel scaffold for integrative osteochondral repair. *Annals of Biomedical Engineering*, *38*(6), 2183–2196. https://doi.org/10.1007/s10439-010-0038-y

Joseph, C. M., Reardon, P. J. T., Konwarh, R., Knowles, J. C., & Mandal, B. B. (2017). Mimicking Hierarchical Complexity of the Osteochondral Interface Using Electrospun Silk-Bioactive Glass Composites. In *ACS Applied Materials and Interfaces* (Vol. 9, Issue 9). https://doi.org/10.1021/acsami.6b16590

Joseph Rey, J. R. H., Chen, Q., Maalihan, R. D., Ren, J., da Silva, Í. G. M., Dugos, N. P., Caldona, E. B., & Advincula, R. C. (2021). 3D printing of biomedically relevant polymer materials and biocompatibility. *MRS Communications*, *11*(2), 197–212. https://doi.org/10.1557/s43579-021-00038-8

Jungst, T., Smolan, W., Schacht, K., Scheibel, T., & Groll, J. (2016). Strategies and Molecular Design Criteria for 3D Printable Hydrogels. *Chemical Reviews*, *116*(3), 1496–1539. https://doi.org/10.1021/acs.chemrev.5b00303

Karageorgiou, V., & Kaplan, D. (2005). Porosity of 3D biomaterial scaffolds and osteogenesis. *Biomaterials*, *26*(27), 5474–5491. https://doi.org/10.1016/j.biomaterials.2005.02.002

Kazemi, M., & Williams, J. L. (2021). Properties of Cartilage–Subchondral Bone Junctions: A Narrative Review with Specific Focus on the Growth Plate. *Cartilage*, *13*(2), 16S-33S. https://doi.org/10.1177/1947603520924776

Khanarian, N. T., Boushell, M. K., Spalazzi, J. P., Pleshko, N., Boskey, A. L., & Lu, H. H. (2014). FTIR-I Compositional Mapping of the Cartilage-to-Bone Interface as a Function of Tissue Region and Age. *Journal of Bone and Mineral Research*, *29*(12), 2643–2652. https://doi.org/10.1002/jbmr.2284

Khanmohammadi, M., Nemati, S., Ai, J., & Khademi, F. (2019). Multipotency expression of human adipose stem cells in filament-like alginate and gelatin derivative hydrogel fabricated through visible light-initiated crosslinking. *Materials Science and Engineering C*, *103*(February), 109808. https://doi.org/10.1016/j.msec.2019.109808

Kim, H. C., Kim, E., Hong, B. M., Park, S. A., & Park, W. H. (2021). Photocrosslinked poly(γ-glutamic acid) hydrogel for 3D bioprinting. *Reactive and Functional Polymers*, *161*(September 2020), 104864. https://doi.org/10.1016/j.reactfunctpolym.2021.104864

Kim, H., Kang, B., Cui, X., Lee, S., Lee, K., Cho, D., Hwang, W., Woodfield, T. B. F., Lim, K. S., & Jang, J. (2021). Light- Activated Decellularized Extracellular Matrix- Based Bioinks for Volumetric Tissue Analogs at the Centimeter Scale. *Advanced Functional Materials*, *31*(32), 2011252. https://doi.org/10.1002/adfm.202011252

Kim, I. L., Mauck, R. L., & Burdick, J. A. (2011). Hydrogel design for cartilage tissue engineering: A case study with hyaluronic acid. *Biomaterials*, *32*(34), 8771–8782. https://doi.org/10.1016/j.biomaterials.2011.08.073

Kim, J. E., Kim, S. H., & Jung, Y. (2016). Current status of three-dimensional printing inks for soft tissue regeneration. *Tissue Engineering and Regenerative Medicine*, *13*(6), 636–646. https://doi.org/10.1007/s13770-016-0125-8

Kolesky, D. B., Truby, R. L., Gladman, A. S., Busbee, T. A., Homan, K. A., & Lewis, J. A. (2014). 3D bioprinting of vascularized, heterogeneous cell-laden tissue constructs. *Advanced Materials*, *26*(19), 3124–3130. https://doi.org/10.1002/adma.201305506

Lee, C. R., Grodzinsky, A. J., & Spector, M. (2001). The effects of cross-linking of collagen-glycosaminoglycan scaffolds on compressive stiffness, chondrocyte-mediated contraction, proliferation and biosynthesis. *Biomaterials*, *22*(23), 3145–3154. https://doi.org/10.1016/S0142-9612(01)00067-9

Lee, F., Chung, J. E., & Kurisawa, M. (2008). An injectable enzymatically crosslinked hyaluronic acid-tyramine hydrogel system with independent tuning of mechanical strength and gelation rate. *Soft Matter*, *4*(4), 880–887. https://doi.org/10.1039/b719557e

Li, C., Ouyang, L., Armstrong, J. P. K., & Stevens, M. M. (2021). Advances in the Fabrication of Biomaterials for Gradient Tissue Engineering. *Trends in Biotechnology*, *39*(2), 150–164. https://doi.org/10.1016/j.tibtech.2020.06.005

Lim, K. S., Abinzano, F., Bernal, P. N., Albillos Sanchez, A., Atienza-Roca, P., Otto, I. A., Peiffer, Q. C., Matsusaki, M., Woodfield, T. B. F., Malda, J., & Levato, R. (2020). One-Step Photoactivation of a Dual-Functionalized Bioink as Cell Carrier and Cartilage-Binding Glue for Chondral Regeneration. *Advanced Healthcare Materials*, *9*(15), 1–13. https://doi.org/10.1002/adhm.201901792

Lim, K. S., Klotz, B. J., Lindberg, G. C. J., Melchels, F. P. W., Hooper, G. J., Malda, J., Gawlitta, D., & Woodfield, T. B. F. (2019a). Visible Light Cross-Linking of Gelatin Hydrogels Offers an Enhanced Cell Microenvironment with Improved Light Penetration Depth. *Macromolecular Bioscience*, *19*(6), 1–14. https://doi.org/10.1002/mabi.201900098

Lim, K. S., Klotz, B. J., Lindberg, G. C. J., Melchels, F. P. W., Hooper, G. J., Malda, J., Gawlitta, D., & Woodfield, T. B. F. (2019b). Visible Light Cross- Linking of Gelatin Hydrogels Offers an Enhanced Cell Microenvironment with Improved Light Penetration Depth. *Macromolecular Bioscience*, *19*(6), 1900098. https://doi.org/10.1002/mabi.201900098

Lim, K. S., Schon, B. S., Mekhileri, N. V., Brown, G. C. J., Chia, C. M., Prabakar, S., Hooper, G. J., & Woodfield, T. B. F. (2016). New Visible-Light Photoinitiating System for Improved Print Fidelity in Gelatin-Based Bioinks. *ACS Biomaterials Science and Engineering*, *2*(10), 1752–1762. https://doi.org/10.1021/acsbiomaterials.6b00149

Lin, T. H., Wang, H. C., Cheng, W. H., Hsu, H. C., & Yeh, M. L. (2019). Osteochondral tissue regeneration using a tyramine-modified bilayered plga scaffold combined with articular chondrocytes in a porcine model. *International Journal of Molecular Sciences*, *20*(2). https://doi.org/10.3390/ijms20020326

Liu, F., Chen, Q., Liu, C., Ao, Q., Tian, X., Fan, J., Tong, H., & Wang, X. (2018). Natural polymers for organ 3D bioprinting. *Polymers*, *10*(11), 1–26. https://doi.org/10.3390/polym10111278

Liu, F., Liu, C., Chen, Q., Ao, Q., Tian, X., Fan, J., Tong, H., & Wang, X. (2018). Progress in organ 3D bioprinting. *International Journal of Bioprinting*, *4*(1), 1–15. https://doi.org/10.18063/IJB.v4i1.128

Mao, Q., Wang, Y., Li, Y., Juengpanich, S., Li, W., Chen, M., Yin, J., Fu, J., & Cai, X. (2020). Fabrication of liver microtissue with liver decellularized extracellular matrix (dECM) bioink by digital light processing (DLP) bioprinting. *Materials Science and Engineering C*, *109*(August 2019), 110625. https://doi.org/10.1016/j.msec.2020.110625

Markstedt, K., Escalante, A., Toriz, G., & Gatenholm, P. (2017). Biomimetic Inks Based on Cellulose Nanofibrils and Cross-Linkable Xylans for 3D Printing. *ACS Applied Materials and Interfaces*, *9*(46), 40878–40886. https://doi.org/10.1021/acsami.7b13400

Markstedt, K., Mantas, A., Tournier, I., Martínez Ávila, H., Hägg, D., & Gatenholm, P. (2015). 3D bioprinting human chondrocytes with nanocellulose-alginate bioink for cartilage tissue engineering applications. *Biomacromolecules*, *16*(5), 1489–1496. https://doi.org/10.1021/acs.biomac.5b00188

Mesallati, T., Buckley, C. T., & Kelly, D. J. (2014). Engineering articular cartilage-like grafts by self-assembly of infrapatellar fat pad-derived stem cells. *Biotechnology and Bioengineering*, *111*(8), 1686–1698. https://doi.org/10.1002/bit.25213

Moreira Teixeira, L. S., Feijen, J., van Blitterswijk, C. A., Dijkstra, P. J., & Karperien, M. (2012). Enzyme-catalyzed crosslinkable hydrogels: Emerging strategies for tissue

engineering. *Biomaterials*, *33*(5), 1281–1290. https://doi.org/10.1016/j.biomaterials.2011.10.067

Moustafa, A. B., & Abd- El- Hakim, A. A. (1977). Sodium bisulfite- initiated polymerization of methyl methacrylate in aqueous medium in the presence of the metal oxides CuO and MnO2. *Journal of Applied Polymer Science*, *21*(4), 905–914. https://doi.org/10.1002/app.1977.070210403

Murphy, C. M., & O'Brien, F. J. (2010). Understanding the effect of mean pore size on cell activity in collagen-glycosaminoglycan scaffolds. *Cell Adhesion and Migration*, *4*(3), 377–381. https://doi.org/10.4161/cam.4.3.11747

Nadernezhad, A., Khani, N., Skvortsov, G. A., Toprakhisar, B., Bakirci, E., Menceloglu, Y., Unal, S., & Koc, B. (2016). Multifunctional 3D printing of heterogeneous hydrogel structures. *Scientific Reports*, *6*(August), 1–12. https://doi.org/10.1038/srep33178

Nguyen, D., Hgg, D. A., Forsman, A., Ekholm, J., Nimkingratana, P., Brantsing, C., Kalogeropoulos, T., Zaunz, S., Concaro, S., Brittberg, M., Lindahl, A., Gatenholm, P., Enejder, A., & Simonsson, S. (2017). Cartilage Tissue Engineering by the 3D Bioprinting of iPS Cells in a Nanocellulose/Alginate Bioink. *Scientific Reports*, *7*(1), 1–10. https://doi.org/10.1038/s41598-017-00690-y

Nieto, D., Marchal Corrales, J. A., Jorge De Mora, A., & Moroni, L. (2020). Fundamentals of light-cell-polymer interactions in photo-cross-linking based bioprinting. *APL Bioengineering*, *4*(4), 1–14. https://doi.org/10.1063/5.0022693

Oliveira Silva, M., Gregory, J. L., Ansari, N., & Stok, K. S. (2020). Molecular Signaling Interactions and Transport at the Osteochondral Interface: A Review. *Frontiers in Cell and Developmental Biology*, *8*(August), 1–12. https://doi.org/10.3389/fcell.2020.00750

Ouyang, L. (2019). *Study on Microextrusion-based 3D Bioprinting and Bioink Crosslinking Mechanisms*.

Ouyang, L., Highley, C. B., Sun, W., & Burdick, J. A. (2017a). A Generalizable Strategy for the 3D Bioprinting of Hydrogels from Nonviscous Photo-crosslinkable Inks. *Advanced Materials*, *29*(8). https://doi.org/10.1002/adma.201604983

Ouyang, L., Highley, C. B., Sun, W., & Burdick, J. A. (2017b). A Generalizable Strategy for the 3D Bioprinting of Hydrogels from Nonviscous Photo-crosslinkable Inks. *Advanced Materials*, *29*(8), 1–7. https://doi.org/10.1002/adma.201604983

Ozbolat, I. T., & Hospodiuk, M. (2016). Current advances and future perspectives in extrusion-based bioprinting. *Biomaterials*, *76*, 321–343. https://doi.org/10.1016/j.biomaterials.2015.10.076

Ozler, S. B., Bakirci, E., Kucukgul, C., & Koc, B. (2017). Three-dimensional direct cell bioprinting for tissue engineering. *Journal of Biomedical Materials Research - Part B Applied Biomaterials*, *105*(8), 2530–2544. https://doi.org/10.1002/jbm.b.33768

Paul, S., & Ranby, B. (1976). *Studies of Methyl Methacrylate-Glycidyl Methacrylate Copolymers: Copolymerization To Low Molecular Weights and Modification By Ring-Opening Reaction of Epoxy Side Groups.* *14*(10), 2449–2461. https://doi.org/10.1002/pol.1976.170141012

Paul, T. K., Sathpathy, U., & Konar, R. S. (1982). Some observations in the aqueous and emulsion polymerizations of common vinyl monomers initiated by sodium metabisulfite (Na2S2O5) at 50°C. *Journal of Applied Polymer Science*, *27*(5), 1501–1511. https://doi.org/10.1002/app.1982.070270509

Pedde, R. D., Mirani, B., Navaei, A., Styan, T., Wong, S., Mehrali, M., Thakur, A., Mohtaram,

N. K., Bayati, A., Dolatshahi-Pirouz, A., Nikkhah, M., Willerth, S. M., & Akbari, M. (2017). Emerging Biofabrication Strategies for Engineering Complex Tissue Constructs. *Advanced Materials*, *29*(19), 1–27. https://doi.org/10.1002/adma.201606061

Pereira, R. F., Sousa, A., Barrias, C. C., Bayat, A., Granja, P. L., & Bártolo, P. J. (2017). Advances in bioprinted cell-laden hydrogels for skin tissue engineering. *Biomanufacturing Reviews*, *2*(1). https://doi.org/10.1007/s40898-017-0003-8

Priya, G., Madhan, B., Narendrakumar, U., Venkata, R., Kumar, S., & Manjubala, I. (2021). *In Vitro and In Vivo Evaluation of Carboxymethyl Cellulose Sca ff olds for Bone Tissue Engineering Applications*. https://doi.org/10.1021/acsomega.0c04551

Prodanovic, O., Spasojevic, D., Prokopijevic, M., Radotic, K., & Markovic, N. (2015). Tyramine modified alginates via periodate oxidation for peroxidase induced hydrogel formation and immobilization. *Reactive and Functional Polymers*, *93*, 77–83. https://doi.org/10.1016/j.reactfunctpolym.2015.06.004

Rapp, T. L., Highley, C. B., Manor, B. C., Burdick, J. A., & Dmochowski, I. J. (2018). Ruthenium-Crosslinked Hydrogels with Rapid, Visible-Light Degradation. *Chemistry - A European Journal*, *24*(10), 2328–2333. https://doi.org/10.1002/chem.201704580

Ribeiro, A., Blokzijl, M. M., Levato, R., Visser, C. W., Castilho, M., Hennink, W. E., Vermonden, T., & Malda, J. (2018). Assessing bioink shape fidelity to aid material development in 3D bioprinting. *Biofabrication*, *10*(1), 1–16. https://doi.org/10.1088/1758-5090/aa90e2

Saghati, S., Nasrabadi, H. T., Khoshfetrat, A. B., Moharamzadeh, K., Hassani, A., Mohammadi, S. M., Rahbarghazi, R., & Fathi Karkan, S. (2021). Tissue Engineering Strategies to Increase Osteochondral Regeneration of Stem Cells; a Close Look at Different Modalities. *Stem Cell Reviews and Reports*, *17*(4), 1294–1311. https://doi.org/10.1007/s12015-021-10130-0

Sakai, S., Ogushi, Y., & Kawakami, K. (2009). Enzymatically crosslinked carboxymethylcellulose-tyramine conjugate hydrogel: Cellular adhesiveness and feasibility for cell sheet technology. *Acta Biomaterialia*, *5*(2), 554–559. https://doi.org/10.1016/j.actbio.2008.10.010

Sakai, S., Ohi, H., Hotta, T., Kamei, H., & Taya, M. (2018). Differentiation potential of human adipose stem cells bioprinted with hyaluronic acid/gelatin-based bioink through microextrusion and visible light-initiated crosslinking. *Biopolymers*, *109*(2), 1–8. https://doi.org/10.1002/bip.23080

Sakai, S., Yamamoto, Y., Enkhtuul, G., Ueda, K., Arai, K., Taya, M., & Nakamura, M. (2017). Inkjetting Plus Peroxidase-Mediated Hydrogelation Produces Cell-Laden, Cell-Sized Particles with Suitable Characters for Individual Applications. *Macromolecular Bioscience*, *17*(5), 1–6. https://doi.org/10.1002/mabi.201600416

Schipani, R., Scheurer, S., Florentin, R., Critchley, S. E., & Kelly, D. J. (2020). Reinforcing interpenetrating network hydrogels with 3D printed polymer networks to engineer cartilage mimetic composites. *Biofabrication*, *12*(3), 035011. https://doi.org/10.1088/1758-5090/ab8708

Schwab, A., Levato, R., D'Este, M., Piluso, S., Eglin, D., & Malda, J. (2020). Printability and Shape Fidelity of Bioinks in 3D Bioprinting. *Chemical Reviews*, *120*(19), 11028–11055. https://doi.org/10.1021/acs.chemrev.0c00084

Setayeshmehr, M., Esfandiari, E., Rafieinia, M., Hashemibeni, B., Taheri-Kafrani, A., Samadikuchaksaraei, A., Kaplan, D. L., Moroni, L., & Joghataei, M. T. (2019). Hybrid and composite scaffolds based on extracellular matrices for cartilage tissue engineering.

*Tissue Engineering - Part B: Reviews*, *25*(3), 202–224. https://doi.org/10.1089/ten.teb.2018.0245

Sheehy, E. J., Mesallati, T., Vinardell, T., & Kelly, D. J. (2015). Engineering cartilage or endochondral bone: A comparison of different naturally derived hydrogels. *Acta Biomaterialia*, *13*, 245–253. https://doi.org/10.1016/j.actbio.2014.11.031

Shi, W., Sun, M., Hu, X., Ren, B., Cheng, J., Li, C., Duan, X., Fu, X., Zhang, J., Chen, H., & Ao, Y. (2017). Structurally and Functionally Optimized Silk-Fibroin-Gelatin Scaffold Using 3D Printing to Repair Cartilage Injury In Vitro and In Vivo. *Advanced Materials*, *29*(29), 1701089. https://doi.org/10.1002/adma.201701089

Shim, J. H., Jang, K. M., Hahn, S. K., Park, J. Y., Jung, H., Oh, K., Park, K. M., Yeom, J., Park, S. H., Kim, S. W., Wang, J. H., Kim, K., & Cho, D. W. (2016). Three-dimensional bioprinting of multilayered constructs containing human mesenchymal stromal cells for osteochondral tissue regeneration in the rabbit knee joint. *Biofabrication*, *8*(1), 14102. https://doi.org/10.1088/1758-5090/8/1/014102

Skardal, A., & Atala, A. (2015). Biomaterials for Integration with 3-D Bioprinting. *Annals of Biomedical Engineering*, *43*(3), 730–746. https://doi.org/10.1007/s10439-014-1207-1

Toprakhisar, B., Nadernezhad, A., Bakirci, E., Khani, N., Skvortsov, G. A., & Koc, B. (2018). Development of Bioink from Decellularized Tendon Extracellular Matrix for 3D Bioprinting. *Macromolecular Bioscience*, *18*(10), 1–12. https://doi.org/10.1002/mabi.201800024

Trabbic-Carlson, K., Setton, L. A., & Chilkoti, A. (2003). Swelling and mechanical behaviors of chemically cross-linked hydrogels of elastin-like polypeptides. *Biomacromolecules*, *4*(3), 572–580. https://doi.org/10.1021/bm025671z

Turunen, S., Kaisto, S., Skovorodkin, I., Mironov, V., Kalpio, T., Vainio, S., & Rak-Raszewska, A. (2018). 3D bioprinting of the kidney—hype or hope? *AIMS Cell and Tissue Engineering*, *2*(3), 119–162. https://doi.org/10.3934/celltissue.2018.3.119

Uludag, H., De Vos, P., & Tresco, P. A. (2000). Technology of mammalian cell encapsulation. *Advanced Drug Delivery Reviews*, *42*(1–2), 29–64. https://doi.org/10.1016/S0169-409X(00)00053-3

Van Den Bulcke, A. I., Bogdanov, B., De Rooze, N., Schacht, E. H., Cornelissen, M., & Berghmans, H. (2000). Structural and Rheological Properties of Methacrylamide Modified Gelatin Hydrogels. *Biomacromolecules*, *1*(1), 31–38. https://doi.org/10.1021/bm990017d

Van Hoorick, J., Tytgat, L., Dobos, A., Ottevaere, H., Van Erps, J., Thienpont, H., Ovsianikov, A., Dubruel, P., & Van Vlierberghe, S. (2019). (Photo-)crosslinkable gelatin derivatives for biofabrication applications. *Acta Biomaterialia*, *97*, 46–73. https://doi.org/10.1016/j.actbio.2019.07.035

van Sliedregt, A., Knook, M., Hesseling, S. C., Koerten, H. K., de Groot, K., & van Blitterswijk, C. A. (1992). Cellular reaction on the intraperitoneal injection of four types of polylactide particulates. *Biomaterials*, *13*(12), 819–824. https://doi.org/10.1016/0142-9612(92)90174-M

Vyas, C., Poologasundarampillai, G., Hoyland, J., & Bartolo, P. (2017). 3D printing of biocomposites for osteochondral tissue engineering. In *Biomedical Composites* (Second Edi). Elsevier Ltd. https://doi.org/10.1016/b978-0-08-100752-5.00013-5

Walker, J. M. (2009). Methods in MOLECULAR BIOLOGY ™ Human Cell Culture Protocols. In *Life Sciences* (Vol. 531, Issue 1).

Wang, L. S., Du, C., Chung, J. E., & Kurisawa, M. (2012). Enzymatically cross-linked gelatin-

phenol hydrogels with a broader stiffness range for osteogenic differentiation of human mesenchymal stem cells. *Acta Biomaterialia*, *8*(5), 1826–1837. https://doi.org/10.1016/j.actbio.2012.02.002

Wang, X. (2019). Advanced polymers for three-dimensional (3D) organ bioprinting. *Micromachines*, *10*(12), 1–26. https://doi.org/10.3390/mi10120814

Wang, X., He, K., & Zhang, W. (2013). Optimizing the fabrication processes for manufacturing a hybrid hierarchical polyurethane-cell/hydrogel construct. *Journal of Bioactive and Compatible Polymers*, *28*(4), 303–319. https://doi.org/10.1177/0883911513491359

Wang, Z., Kumar, H., Tian, Z., Jin, X., Holzman, J. F., Menard, F., & Kim, K. (2018). Visible Light Photoinitiation of Cell-Adhesive Gelatin Methacryloyl Hydrogels for Stereolithography 3D Bioprinting. *ACS Applied Materials and Interfaces*, *10*(32), 26859–26869. https://doi.org/10.1021/acsami.8b06607

Wei, M., Hsu, Y. I., Asoh, T. A., Sung, M. H., & Uyama, H. (2021). Injectable poly(γ-glutamic acid)-based biodegradable hydrogels with tunable gelation rate and mechanical strength. *Journal of Materials Chemistry B*, *9*(16), 3584–3594. https://doi.org/10.1039/d1tb00412c

Wei, S. M., Pei, M. Y., Pan, W. L., Thissen, H., & Tsai, S. W. (2020). Gelatin hydrogels reinforced by absorbable nanoparticles and fibrils cured in situ by visible light for tissue adhesive applications. *Polymers*, *12*(5), 1–14. https://doi.org/10.3390/POLYM12051113

Wei, W., & Dai, H. (2021). Articular cartilage and osteochondral tissue engineering techniques: Recent advances and challenges. *Bioactive Materials*, *6*(12), 4830–4855. https://doi.org/10.1016/j.bioactmat.2021.05.011

Wu, Yanbin, Joseph, S., & Aluru, N. R. (2009). Effect of cross-linking on the diffusion of water, ions, and small molecules in hydrogels. *Journal of Physical Chemistry B*, *113*(11), 3512–3520. https://doi.org/10.1021/jp808145x

Wu, Yun, Lin, Z. Y. (William), Wenger, A. C., Tam, K. C., & Tang, X. (Shirley). (2018). 3D bioprinting of liver-mimetic construct with alginate/cellulose nanocrystal hybrid bioink. *Bioprinting*, *9*(August 2017), 1–6. https://doi.org/10.1016/j.bprint.2017.12.001

Xiao, W., He, J., Nichol, J. W., Wang, L., Hutson, C. B., Wang, B., Du, Y., Fan, H., & Khademhosseini, A. (2011). Synthesis and characterization of photocrosslinkable gelatin and silk fibroin interpenetrating polymer network hydrogels. *Acta Biomaterialia*, *7*(6), 2384–2393. https://doi.org/10.1016/j.actbio.2011.01.016

Yuan, X. L., Meng, H. Y., Wang, Y. C., Peng, J., Guo, Q. Y., Wang, A. Y., & Lu, S. B. (2014). Bone-cartilage interface crosstalk in osteoarthritis: Potential pathways and future therapeutic strategies. *Osteoarthritis and Cartilage*, *22*(8), 1077–1089. https://doi.org/10.1016/j.joca.2014.05.023

Zhang, B., Huang, J., & Narayan, R. J. (2020). Gradient scaffolds for osteochondral tissue engineering and regeneration. *Journal of Materials Chemistry B*, *8*(36), 8149–8170. https://doi.org/10.1039/d0tb00688b

Zheng, C., & Levenston, M. (2015). FACT VERSUS ARTIFACT: AVOIDING ERRONEOUS ESTIMATES OF SULFATED GLYCOSAMINOGLYCAN CONTENT USING THE DIMETHYLMETHYLENE BLUE COLORIMETRIC ASSAY FOR TISSUE-ENGINEERED CONSTRUCTS. *European Cells & Materials*, *29*, 224–236.

Zheng, Z., Eglin, D., Alini, M., Richards, G. R., Qin, L., & Lai, Y. (2021). Visible Light-Induced 3D Bioprinting Technologies and Corresponding Bioink Materials for Tissue Engineering: A Review. *Engineering*, *7*(7), 966–978. https://doi.org/10.1016/j.eng.2020.05.021

Zhong, Y., Wang, J., Yuan, Z., Wang, Y., Xi, Z., Li, L., Liu, Z., & Guo, X. (2019). A mussel-inspired carboxymethyl cellulose hydrogel with enhanced adhesiveness through enzymatic crosslinking. *Colloids and Surfaces B: Biointerfaces*, *179*(December 2018), 462–469. https://doi.org/10.1016/j.colsurfb.2019.03.044

Zuscik, M. J., Hilton, M. J., Zhang, X., Chen, D., & O'Keefe, R. J. (2008). Regulation of chondrogenesis and chondrocyte differentiation by stress. *Journal of Clinical Investigation*, *118*(2), 429–438. https://doi.org/10.1172/JCI34174